Dalton Transactions

ROYAL SOCIETY OF CHEMISTRY

PAPER

View Article Online
View Journal | View Issue

Cite this: *Dalton Trans.*, 2025, **54**, 728

Distinguishing between aquo and hydroxo coordination in molecular copper complexes by ^{1}H and ^{17}O ENDOR spectroscopy†

Julia Haak[a,b] and George E. Cutsail III *[a,b]

Aquo and hydroxo ligands play an essential role in the chemistry of many copper enzymes and small molecule catalysts. The formation of a series of copper complexes with H_2O and OH^- ligands in various positions, including $[Cu(bpy)(OAc)(H_2O)_{2,ax}]^+$ (**Cu-I**), $[Cu(bpy)(OH)_{2,eq}(H_xO)_{2,ax}]$ (**Cu-III**), $[Cu(OH)_{4,eq}(H_xO)_{2,ax}]^{2-}$ (**Cu-IV**), $[Cu(bpy)(H_2O)_{2,eq}(H_2O)_{2,ax}]^{2+}$ (**Cu-V**) and $[Cu(bpy)_2(H_2O)_{ax}]^{2+}$ (**Cu-VI**), were investigated through Electron Paramagnetic Resonance (EPR) and UV-Vis spectroscopy in aqueous copper bipyridine solutions in the dependence of the pH and the copper-to-bipyridine ratio (bpy = 2,2′-bipyridine). ^{2}H- and ^{17}O-enrichment of the copper complexes allowed us to determine the ^{1}H and ^{17}O nuclear hyperfine interactions of their H_xO ligands *via* Q-band Electron Nuclear Double Resonance (ENDOR) spectroscopy. These techniques gave direct insight into the metal–ligand covalencies and geometries and were further supported by Density Functional Theory (DFT) calculations. It is shown that ^{1}H and ^{17}O ENDOR spectroscopy can aid in (1) determining the coordination position, thereby differentiating between equatorial and axial H_xO ligands and (2) distinguishing equatorial aqua and hydroxo ligands, particularly through their anisotropic dipolar components. We further studied the influence of *trans* coordinating ligands on the hyperfine parameters of aquo and hydroxo ligands, enabled through contrasting the coordination environments in the examined complexes, supported by quantum chemical computations.

Received 24th September 2024,
Accepted 12th November 2024

DOI: 10.1039/d4dt02708f

rsc.li/dalton

Introduction

The ability of monocopper active sites to catalyze both the activation of molecular oxygen, on the one hand, and the formation of the O–O bond in dioxygen, on the other hand, is of fundamental importance to numerous catalytic processes. In nature, dopamine β-monooxygenase (DβM) and peptidylglycine α-amidating monooxygenase (PHM) use molecular oxygen to selectively hydroxylate secondary C–H bonds (under production of water) at uncoupled dinuclear copper sites, where the activation of dioxygen occurs categorically at a single copper center.[1] Other prominent monooxygenases such as lytic polysaccharide monooxygenase (LPMO) that catalyzes the oxidative depolymerization of polysaccharides[2,3] and particulate methane monooxygenase (pMMO) that oxidizes methane to methanol[4] have been demonstrated to use dioxygen as a co-substrate at monocopper active sites, two reactions that play crucial roles in the production of renewable energy and thereby the reduction of greenhouse gases.

In materials science research, the intriguing redox chemistry of copper enzymes has drawn considerable interest, which led to the development of a variety of synthetic heterogeneous and homogeneous copper catalysts over the past decades, for example for oxidative C–H functionalizations.[5] Copper-exchanged zeolites have proved to be especially interesting for the conversion of methane to methanol, mimicking pMMO's reactivity.[6] More recent studies have targeted copper active site designs in metal–organic frameworks (MOFs) to mimic biologically active sites and control catalysis.[7,8]

By means of O–O bond formation, a variety of heterogeneous and homogeneous catalysts for electrochemical water oxidation have also been designed.[9–18] The first homogeneous copper water oxidation catalyst (WOC) was reported in 2012 by the group of Mayer, demonstrating the catalytic activity of the copper bipyridine system (1 : 1 M : L ratio) at a high pH value.[10] At pH values between pH 11.8 and 13.3 electrochemical water oxidation occurs with high turnover frequencies of ~100 s^{-1}.

[a]*Max Planck Institute for Chemical Energy Conversion, Stiftstraße 34-36, D-45470 Mülheim an der Ruhr, Germany. E-mail: george.cutsail@cec.mpg.de*
[b]*Institute for Inorganic Chemistry, University of Duisburg-Essen, Universitätsstraße 5–7, 45117 Essen, Germany*

†Electronic supplementary information (ESI) available: Additional experimental details including spectrometer conditions, UV-Vis spectra, cyclic voltammograms, multi-frequency EPR spectra, ^{14}N ENDOR spectra, room temperature EPR pH titration, ^{1,2}H ENDOR subtractions with simulations, ^{14}N/^{17}O ENDOR subtractions, EDNMR spectra, and computational details including coordinates of DFT optimized structures. Additional citations are made within the ESI.[82,83] See DOI: https://doi.org/10.1039/d4dt02708f

This work has inspired more mechanistic and theoretical studies of the parent copper bipyridine system and its substituted modifications, which are generally all catalytically active in aqueous solutions and have exchangeable water or hydroxo ions that occupy an open coordination site.[13,15,17,19–21] These exchangeable ligands are readily displaced upon reduction of the Cu(II) center to Cu(I) to allow for O_2 or H_2O_2 binding, accompanied by re-oxidation of the metal center to a Cu(II) state. For various copper WOCs, the coordinated hydroxo ion is suggested to play a direct role in the formation of O_2 and its incorporation into the product.[15,19]

EPR spectroscopy allows one to obtain information on the general coordination environment, the electronic configuration and the nuclearities (*e.g.* dimerization) of paramagnetic metal centers. For monocopper(II) active sites, a d^9 S = 1/2 electronic configuration yields an EPR spectrum that directly shows the ground state configuration of the singly occupied molecular orbital (SOMO), distinguishing $d_{x^2-y^2}$ from d_{z^2} ground-states by the $\boldsymbol{g}$-tensor ($d_{x^2-y^2}$: $g_\parallel > g_\perp$; d_{z^2}: $g_\perp > g_\parallel$). The copper hyperfine interaction, which is commonly observed by EPR spectroscopy, is a reporter of the ligand field of the copper center and gives estimates on the degree of spin delocalization onto ligands. More detailed electronic and geometric information is encoded in the magnitude and orientation of nuclear superhyperfine interactions of the ligand nuclei, which sometimes may be resolved by EPR spectroscopy directly. In copper bpy complexes, the ^{14}N couplings of the bpy ligands are often at least partly observed, which allows for estimates on the magnitude of hyperfine interactions.[22] The determination of the ligand's full hyperfine tensor from EPR alone can be challenging and in many cases unfeasible, requiring the application of more advanced EPR techniques. The EPR linewidth of metal centers, including copper, is often significantly broadened by numerous possible influences, including other numerous weaker hyperfine interactions and/or strain effects, which effectively conceal the hyperfine interactions of weakly coupled nucleus like protons. To resolve such couplings, the use of hyperfine techniques like ENDOR spectroscopy is required. The understanding and benchmarking of ^1H couplings are critical for the distinction between various ligands, specifically water and hydroxo, and even their coordination positions (*i.e.* equatorial *vs.* axial).

The interaction of the copper center with exchangeable oxygen ligands (water and hydroxo ions) holds great information on the exact nature of the ligands, covalencies, distances and geometries. While there are various past studies and assignments on the protons of these H_xO ligands,[23–30] direct studies of the oxygen hyperfine interaction are less common and are less systematically understood. Oxygen has only one NMR-active isotope, ^{17}O, with a nuclear spin of I = 5/2, which has a very low natural abundance (0.038%), thus requiring any potential EPR and hyperfine measurements to use ^{17}O enrichment. In terms of ^{17}O hyperfine studies of copper systems, they are still relatively rare in comparison with other nuclei, despite the numerous catalytic processes that invoke oxygen ligands.[30–34]

Herein, we have set out to understand the ligand hyperfine interactions of aqua and hydroxo copper complexes *via* both ^1H and ^{17}O ENDOR spectroscopy to understand the hyperfine and structural relationship of these ligands. To systematically understand these interactions, we have characterized a range of well-studied copper bpy complexes to survey how changes in the ligand sphere change the spectroscopic footprint of the respective H_xO ligand. This system was chosen not simply for its relevance to water oxidation catalysis, but also for its ease of preparation (low $H_2{}^{17}O$ requirements) and variety of oxygen ligand conformers.

Based on previous studies,[22,35–47] it was expected that the bis-aqua complex $[Cu(bpy)(H_2O)_2]^{2+}$ forms upon mixing of bpy and a copper source near neutral pH.[10] As the pH is then increased, this species is suggested to transform *via* the EPR-silent dimeric $[Cu(bpy)(OH)]_2{}^{2+}$ at intermediate pH values into the bis-hydroxo complex $[Cu(bpy)(OH)_2]$ at further elevated pH, which was assumed to be the water oxidation catalyst (Scheme 1).

In this study, we applied UV-Vis, EPR, ENDOR and ELDOR-Detected NMR (EDNMR) spectroscopy, in combination with DFT calculations to shed further light on the nature of the pH-dependent equilibria and the evolving complexes. Most importantly, we take advantage of the simplicity of the copper bpy system to purposefully study the ligand superhyperfine interactions in various water-derived ligands. Employment of ^{17}O-enriched water allows not only the study of ^1H couplings, but also the direct interaction of the ^{17}O nucleus of H_2O and OH^- ligands with the metal center.

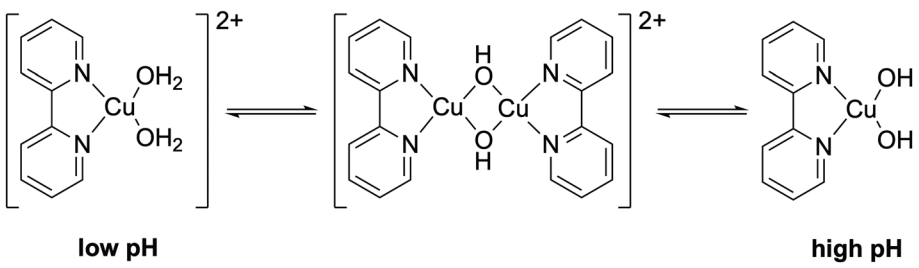

Scheme 1 Proposed pH dependent structures of copper bpy (1 : 1) complexes.

Methods and materials

Sample preparation

Aqueous solutions of copper bpy complexes were prepared by mixing one equivalent of 2,2′-bipyridine (Sigma Aldrich) with one equivalent of $Cu(OAc)_2 \cdot H_2O$ (Sigma Aldrich) in water, or in the case of **Cu-VI** by mixing both components in a 2 : 1 ratio. If not mentioned otherwise, $NaOAc \cdot 3H_2O$ (Alfa Aesar) was added to a final concentration of 0.1 M. For **Cu-V** 30% v/v glycerol was used instead of sodium acetate. ^{17}O- and ^{2}H-enriched samples were prepared in $H_2{}^{17}O$ (90 atom%, Sigma Aldrich) or D_2O (99.95 atom%, Deutero). pH values were adjusted with solutions of NaOH (prepared from pellets; Alfa Aesar) either with an InLab Versatile Pro or an InLab Micro Pro-ISM pH electrode (Mettler-Toledo), calibrated by four-point calibration in the range of pH 4 to 13.

UV-Vis spectroscopy

UV-Vis spectra were recorded with a Cary 60 UV-Vis spectrophotometer from Agilent using Hellma quartz cuvettes (quartz glass of high performance purity) with a path length of 1 cm. Spectra were recorded on copper bpy solutions of concentrations of 10 mM.

Cyclic voltammetry

Cyclic voltammograms were obtained using a VersaSTAT4 potentiostat with a platinum auxiliary electrode, a 3 mm diameter glassy carbon working electrode and an Ag/AgCl (3 M KCl) reference electrode (all electrodes from BASi). 0.1 M NaOAc was used as an electrolyte.

CW X-band EPR spectroscopy

Continuous-wave X-band EPR spectra were recorded using a Bruker MS5000 spectrometer. The samples that were recorded at room temperature contained 10 mM copper bpy solutions, filled in 50 μL capillaries (Hirschmann). Samples between pH 6.1 and 12.7 were produced *via* pH titrations (pH adjustments with NaOH, see above). The spectrometer conditions applied for all samples are reported in Table S1.† For measurements at cryogenic temperatures a liquid nitrogen cryostat or a finger dewar was employed and custom quartz EPR tubes with 4 mm outer diameter (OD) were filled with 1 mM solutions and frozen. The spectrometer conditions for these measurements are reported in Table S2.†

Pulsed Q-band EPR and ENDOR spectroscopy

Q-band EPR and ENDOR spectra were recorded using 1 mM solutions in 2.8 mm OD custom quartz tubes with a Bruker Elexsys E580 spectrometer equipped with home-built up/down Q-band conversion accessories,[48] an Oxford CF935 helium flow cryostat and temperature controller, and a cylindrical TE_{011} microwave resonator.[49] Two-pulse (Hahn) echo detected Q-band EPR spectra were recorded with a $\pi/2$–τ–π–τ–echo pulse sequence and Davies[50] ENDOR experiments employed a π–T_{RF}–t_{wait}–$\pi/2$–τ–π–τ–echo sequence, where the radio frequency (RF) pulse is applied during time T_{RF} and the RF was randomly hopped[51] without phase cycling. The spectrometer conditions for the individual experiments are reported in Tables S3–S5.†

Pulsed W-band EPR and EDNMR spectroscopy

W-band pulsed spectra were recorded using 1 mM solutions filled in 0.9 OD custom quartz tubes and collected on a Bruker Elexsys E680 spectrometer equipped with a closed cycle helium cryostat system. For EPR measurements, a two-pulse (Hahn) sequence of $\pi/2$–τ–π–τ–echo was employed. The magnet was swept up and down and the offsets were averaged to correct for sweep delays. EDNMR spectra[52] were recorded using a t_{HTA}–t_{wait}–$\pi/2$–τ–π–τ–echo sequence, where t_{HTA} is the length of the high turning angle pulse and t_{wait} is the time between the HTA pulse and the echo detection. The spectrometer conditions for the individual experiments are reported in Tables S6 and S7.†

Raw data were processed and analyzed in Matlab R2023a and simulated using the EasySpin package (v. 6.0.0-dev. 51).[53] EDNMR simulations were obtained using the function *horseradish*.[54]

DFT calculations

All calculations were performed with the Orca quantum chemistry software (v. 5.0),[55,56] taking dispersion effects into account by utilizing Grimme's D3 correction with Becke–John damping.[57,58] Solvation effects (water) were included with the conductor-like polarizable continuum model (CPCM)[59] and relativistic effects were treated at the level of zeroth order regular approximation (ZORA).[60–62] Geometry optimizations were carried out using the BP86 functional,[63,64] while the B3LYP functional[65,66] was used for the determination of the EPR parameters. The all-electron def2-TZVP basis set[67,68] was employed, with the exception of the calculation of EPR parameters, where the epr-III basis set[69,70] was used for all hydrogens and the aug-cc-pVTZ-J basis set for copper.[71,72] For all calculations automatically generated auxiliary basis sets were applied (AutoAux).[73]

Results and discussion

Catalytic activity and UV-Vis and EPR spectroscopy

Copper bpy complexes were prepared as described for the water oxidation experiments reported by Barnett *et al.* by mixing one equivalent of bipyridine ligand with one equivalent of copper acetate.[10] To understand the system as previously reported, we prepared all samples with 0.1 M sodium acetate electrolyte, unless noted otherwise. We did find that the addition of the electrolyte aided as a glassing agent during the freezing of EPR samples (Fig. S1†). Spectrophotometric pH titrations of the 1 : 1 Cu : bpy solution have a similar result to what has previously been reported.[22] Briefly, the color of the solution changes from light blue (pH 6.5, λ_{max} = 668 nm, and ε = 37 M^{-1} cm^{-1}) to a darker blue at a high pH value (pH = 12, λ_{max} = 615 nm, ε = 41 M^{-1} cm^{-1}), as shown in Fig. 1. The blue

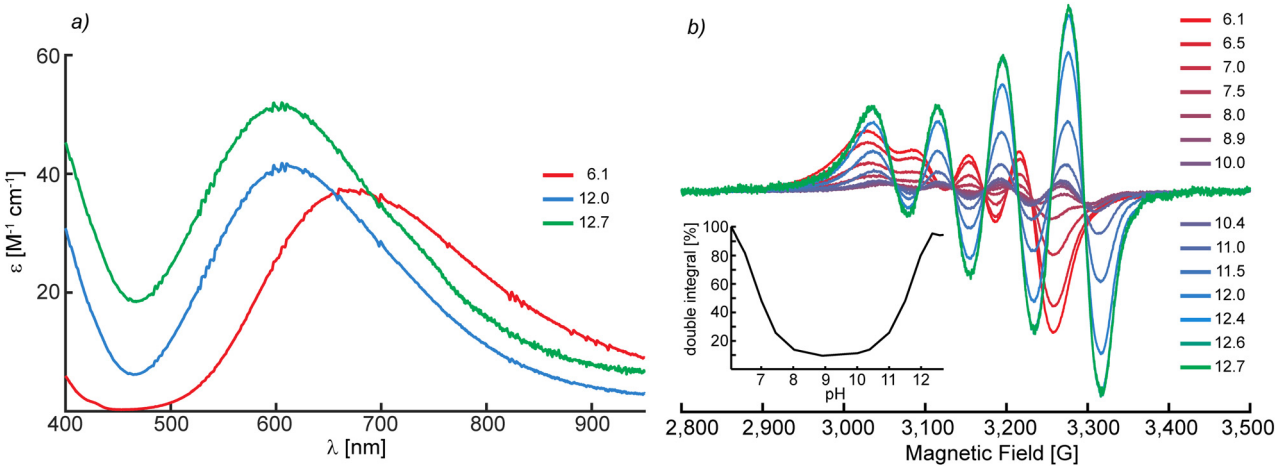

Fig. 1 Spectroscopic investigations of copper bpy solutions at several pH values showing (a) the shifting d–d transitions in the UV-Vis spectra and (b) the CW X-band (~9.5 GHz) EPR spectra recorded at room temperature. The relative amount of paramagnetic species at the individual pH points was obtained from the double integral of the EPR spectra and is added as an inset. Experimental conditions are reported in the Experimental section.

shift is analogous to the spectra obtained by Garribba *et al.* and consistent with the equilibrium shift from $[Cu(bpy)(H_2O)_2]^{2+}$ to $[Cu(bpy)(OH)_2]$.[22]

At even higher pH values, the spectral character does not change significantly (pH = 12.7, λ_{max} = 605 nm, and ε = 52 M^{-1} cm^{-1}); however, the overall background intensity increases, leading to a higher effective absorptivity and the lack of clear isosbestic points (Fig. S2†). This is most likely related to the observable formation of a dark precipitate at high pH values, which was reported before.[74] The formation of these insoluble copper species (possibly copper oxides) and their consecutive deposition on the cuvette then leads to diffuse scattering and a systematic increase (and error) of the measured absorptivity. However, Barnett *et al.* showed that the active catalyst in their water oxidation reactions is a homogeneous one, indicating that the formed precipitate does not play a significant role in catalysis, but rather represents a decomposition product.[10]

At pH $\gtrsim$ 12 catalytically active solutions were obtained, as seen by large, irreversible oxidation waves (Fig. S3†), in good agreement with what has been described by Barnett *et al.*[10]

The Cu(II) complexes were further investigated by X-band (~9.43 GHz) EPR spectroscopy. The spectra recorded at room temperature are shown in Fig. 1b. The approximately isotropic spectra of the rapidly tumbling molecular solutions at low to neutral pH (pH 6.1–7.0) exhibit a signal centered at g_{iso} ~ 2.15, split to a quartet caused by the electron-nuclear hyperfine interaction of the ^{63,65}Cu isotopes (I = 3/2), $a_{iso}(^{63,65}Cu)$. As the pH is further increased, the quartet signal intensity decreases, before the appearance of a new quartet signal at high pH values with a slightly lower g_{iso} value of ~2.12 and a larger $|a_{iso}|$-value. The double integration of the collected spectra quantifies a maximum signal reduction of 90% at pH 8.9, Fig. 1b. This is explained by the formation of an EPR silent species. The three species identified at neutral, intermediate and high pH values are termed **Cu-I**, **Cu-II** and **Cu-III**, and are assumed to be $[Cu(bpy)(H_2O)_2]^{2+}$, the EPR silent dimer $[Cu(bpy)(\mu\text{-}OH)]_2^{2+}$ and $[Cu(bpy)(OH)_2]$, as assigned previously (Scheme 1).[10,22,37]

The room temperature spectra are not fully isotropic, but exhibit a slightly anisotropic character due to the slow tumbling rate on the timescale of the EPR experiment (10^{-11} s). To accurately simulate the room temperature spectra, the complete spin Hamiltonian must be known, which was estimated from the frozen solution (solid state, powder) EPR spectra, shown in Fig. 2. All frozen solutions exhibit axial EPR spectra, typical of type-2 copper with a $d_{x^2-y^2}$ ground state, with some of them also exhibiting resolved nitrogen superhyperfine interaction ($I(^{14}N)$ = 1/2) of the bpy ligand along $g_\perp$. Collecting EPR spectra at several frequencies (X-, Q- and W-band frequency) and globally fitting the multifrequency EPR spectra (Fig. S4–S9†) yields simulations that excellently reproduce the spectra, including the nitrogen superhyperfine interaction – when available (Fig. 2 and Table 1). The ^{14}N superhyperfine assignments were further confirmed by orientation-selective ^{14}N Davies ENDOR experiments (see below).

The low temperature EPR spectra of copper bpy solutions at moderate pH (pH 6–7) can be simulated with a mostly axial $\boldsymbol{g}$-tensor ($g_\parallel = g_1 > g_\perp = g_2 = g_3$) with a small rhombic splitting, $\boldsymbol{g}^{\mathbf{Cu\text{-}I}}$ = [2.278, 2.068, 2.055], and an axial hyperfine tensor ($\boldsymbol{A}$ = [A_1, A_2, A_3]) of $\boldsymbol{A}^{\mathbf{Cu\text{-}I}}(^{63}Cu)$ = [525, 43, 36] MHz. At pH 12, a single species with a larger $A_\parallel(^{63}Cu)$ value of 560 MHz and overall lower g-values is observed ($\boldsymbol{g}^{\mathbf{Cu\text{-}III}}$ = [2.254, 2.055, 2.050]).

With $\boldsymbol{g}$- and $\boldsymbol{A}(^{63}Cu)$-tensor estimates from the frozen solution EPR spectra, we are now able to simulate the slow-motional regime room temperature EPR spectra (Fig. 2 and Table 1). The room temperature spectra at pH $\leq$ 6.5, and also at pH 12.4, are well reproduced by simulation by considering only a single set of spin Hamiltonian parameters for each. The EPR spectra at pH values between pH 6.5 and pH 12.0 can be

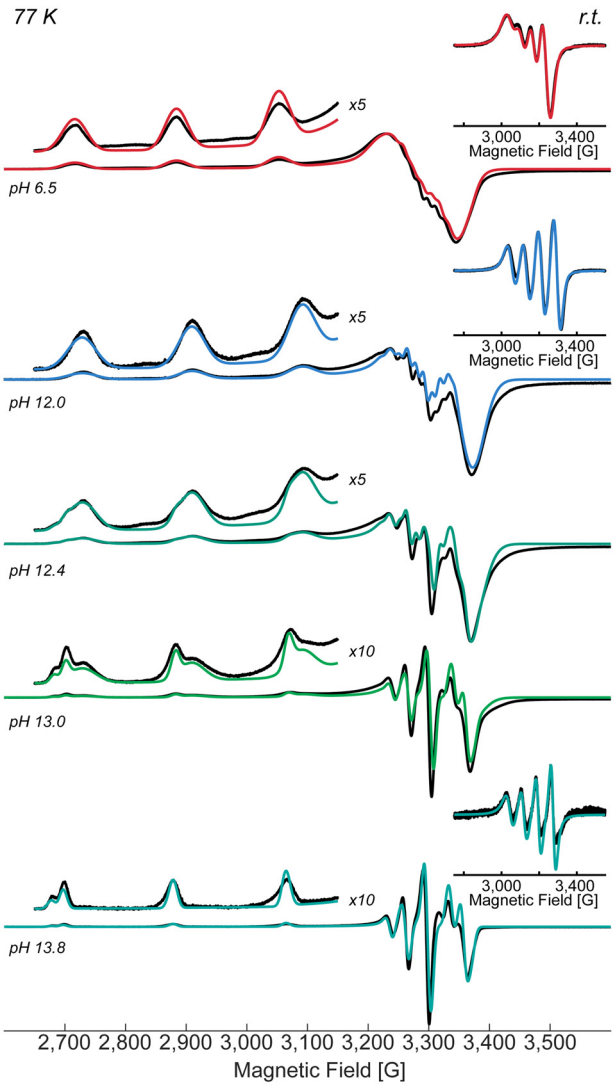

Fig. 2 CW X-band (~9.5 GHz) EPR spectra of copper bpy solutions at several pH values collected at 77 K with an enlargement of the copper hyperfine in the $g_{\|}$ region in black with simulations in color. Spectra of the solutions at room temperature (r.t.) with simulations are added as inserts for three pH values. Experimental conditions are reported in the Experimental section. Simulation parameters are listed in Table 1.

reproduced as mixtures of the **Cu-I** and **Cu-III** components (Fig. S10†). However, at intermediate pH values larger deviations between the simulation and experiment are observed, which implies the formation of additional EPR active species together with dimer formation. Nevertheless, our simulations still are in reasonable agreement with the experimental spectra, which indicates that **Cu-I** and **Cu-III** are the two major EPR active species between pH 7 and pH 12.

While the solid-state simulations do not provide the possibility to determine the *absolute or relative* signs of the individual hyperfine components, the *relative* hyperfine signs are determinable from the simulation of the room temperature EPR spectrum. By making $A_{\|}(^{63}\mathrm{Cu})$ negative, as expected for a type-2 copper, the simulation parameters of the room temperature spectrum of **Cu-I** reveal a slight but necessary rhombic splitting of the $A_{\perp}$(Cu) values in order to accurately reproduce the experiment and yield the observed isotropic hyperfine splitting pattern, Fig. S10.† Therefore, the copper hyperfine of **Cu-I** is either $\boldsymbol{A}^{\mathbf{Cu\text{-}I}}(^{63}\mathrm{Cu})$ = [−525, +43, −36] MHz or [−525, −43, +36] MHz, where the former is only slightly favored, Fig. S11.†

The spin Hamiltonian parameters of both complexes are in good agreement with the ones obtained from simulations of the room temperature spectra (Table 1). For **Cu-I**, slightly lower individual g- and g_{iso}-values at low temperatures are observed compared to the ones determined at room temperature. There is no difference observed between the room temperature and low temperature samples of **Cu-III**. Generally, **Cu-III** exhibits a smaller g_{iso} and larger hyperfine splitting than **Cu-I**. The trend of a reduced $g_{\|}$ and increased $A_{\|}$ for **Cu-III** compared to **Cu-I** reflects the findings of Garribba *et al.* that showed the same trends for the species they assign to be $[\mathrm{Cu(bpy)(H_2O)_2}]^{2+}$ ($g_{\|}$ = 2.307 and $A_{\|}$ = 510 MHz) and $[\mathrm{Cu(bpy)(OH)_2}]$ ($g_{\|}$ = 2.232 and $A_{\|}$ = 588 MHz),[22] where ethylene glycol was used as a glassing agent rather than the sodium acetate reported here.

Notably, when the pH is further increased, the CW X-band EPR spectra of the frozen solutions show the formation of an additional species at higher pH values (Fig. 2). The amount of this species increases as the pH is taken up further until it is the only detected species at pH 13.7 (**Cu-IV**). The spectrum of **Cu-IV** is best simulated with an axial g-tensor ($\boldsymbol{g}^{\mathbf{Cu\text{-}IV}}$ = [2.272, 2.053, 2.050]) and large copper hyperfine ($\boldsymbol{A}^{\mathbf{Cu\text{-}IV}}(^{63}\mathrm{Cu})$ = [−582, −90, −92] MHz). It lacks any resolved ^{14}N hyperfine coupling in the $g_{\perp}$ region and exhibits significantly narrower lines, particularly along $g_{\|}$. This is especially pronounced at the copper hyperfine transition at 2680 G which is much narrower than in **Cu-I** and **Cu-III** which allows to resolve two sharp features, corresponding to transitions of the ^{63}Cu and ^{65}Cu isotopes. The dramatic EPR linewidth sharpening and the loss of ^{14}N hyperfine coupling are attributed to the loss of the bpy ligand. The formation of the tetra hydroxide complex $[\mathrm{Cu(OH)_4}]^{2-}$ is therefore expected, and the spectrum is in very good agreement with the spectrum of $[\mathrm{Cu(OH)_4}]^{2-}$ reported by Chao *et al.* ($\boldsymbol{g}$ = [2.252, 2.050, 2.046]; $A_{\|}$ = 558 MHz; $A_{\perp}$ = 89 MHz).[75] The spectrum of **Cu-IV** obtained at room temperature is well reproduced by a simulation with spin Hamiltonian parameters, which are in good agreement with the ones obtained at low temperature (Fig. S10†). However, a slightly lower copper hyperfine is applied (Table 1).

^{1}H ENDOR spectroscopy

To characterize the H_xO ligands of the presented copper complexes, Q-band pulsed Davies ENDOR experiments were conducted and the ligand superhyperfine couplings were determined. The ^{1}H Davies ENDOR spectra of the copper complexes are displayed in Fig. S12–S16.† The spectra exhibit a multitude of doublets that are centered at the nuclear Larmor frequency ν_{n} and split by the effective, orientation-selective hyperfine coupling A, as expected for weakly coupled nuclei ($|A| < 2|\nu_{\mathrm{n}}|$; $\nu_{\mathrm{n}}(^1\mathrm{H}) \sim 51$ MHz at 12 000 G). The complex ^{1}H ENDOR pattern

Table 1 Summary of spin Hamiltonian parameters for **Cu-I**, **Cu-III** and **Cu-IV** obtained through EPR simulations together with the estimated uncertainties for some parameters. The full parameters are reported in Tables S8 (frozen solution) and S10† (room temperature). Within the scope of this study the three complexes are assigned to be $[Cu(bpy)(OAc)(H_2O)_{2,ax}]^+$, $[Cu(bpy)(OH)_{2,eq}(H_xO)_{2,ax}]$ and $[Cu(OH)_{4,eq}(H_xO)_{2,ax}]^{2-}$, respectively

	Cu-I	Cu-III	Cu-IV
Simulation parameters of frozen solution spectra			
$\boldsymbol{g} = [g_1, g_2, g_3]$	[2.278 ± 0.001, 2.068 ± 0.003, 2.055 ± 0.001]	[2.254 ± 0.001, 2.055 ± 0.001, 2.050 ± 0.002]	[2.272 ± 0.0005, 2.053 ± 0.0005, 2.050 ± 0.0005]
g_{iso} [a]	2.134	2.120	2.125
$\boldsymbol{A}(^{63}Cu) = [A_1, A_2, A_3]$ in MHz [b]	[525 ± 7, 43 ± 10, 36 ± 10]	[560 ± 5, 64 ± 10, 62 ± 10]	[582 ± 4, 90 ± 5, 92 ± 5]
Simulation parameters of room temperature spectra			
$\boldsymbol{g} = [g_1, g_2, g_3]$	[2.284, 2.074, 2.061]	[2.254, 2.055, 2.050]	[2.277, 2.058, 2.055]
g_{iso} [a]	2.140	2.120	2.130
$\boldsymbol{A}(^{63}Cu) = [A_1, A_2, A_3]$ in MHz [b]	[−525, +43, −36]	[−560, −64, −62]	[−582, −40, −40]
$a_{iso}(^{63}Cu)$ in MHz [a]	−173	−229	−221
Rotational correlation time in s (isotropic)	$(3.5 \pm 0.3) \times 1 \times 10^{-11}$	$(2.5 \pm 0.4) \times 1 \times 10^{-11}$	$(2 \pm 0.6) \times 1 \times 10^{-11}$

[a] The isotropic components of the $\boldsymbol{g}$- and $\boldsymbol{A}$-tensors are calculated as follows: $a_{iso} = \frac{A_1 + A_2 + A_3}{3}$ and $g_{iso} = \frac{g_1 + g_2 + g_3}{3}$. [b] Copper hyperfine couplings are reported for the ^{63}Cu isotope. Simulations consider also the ^{65}Cu isotope with hyperfine couplings that are scaled by the gyromagnetic ratio of both nuclei: $\gamma = \frac{|g_n(^{63}Cu)|}{|g_n(^{65}Cu)|} = \frac{|A(^{63}Cu)|}{|A(^{65}Cu)|}$.

originates from a large number of exchangeable protons of the water/hydroxo ligands and non-exchangeable protons of the bpy ligand. To identify the exchangeable H_xO protons, solvent-exchanged samples in D_2O were prepared and the difference in the spectra was calculated (Fig. S12–S16†). A selection of difference spectra along with their simulations are displayed in Fig. 3. We note that the ^1H ENDOR spectra of **Cu-IV** in H_2O are dramatically simplified compared to all other complexes because of the loss of the bpy ligand. Hence, the corresponding ^1H ENDOR spectra of the D_2O solvent exchanged sample had an extremely ^1H weak ENDOR response, as all of the protons in **Cu-IV** are exchangeable.

In the ^1H difference spectra of **Cu-I**, a single sharp ^1H doublet of $A_\perp$ = 3 MHz is observed along $g_\perp$ that broadens to a single doublet of approximately $A_\parallel \sim 7$ MHz. The 2D field-frequency ENDOR pattern of the exchangeable ^1H signal of **Cu-I**

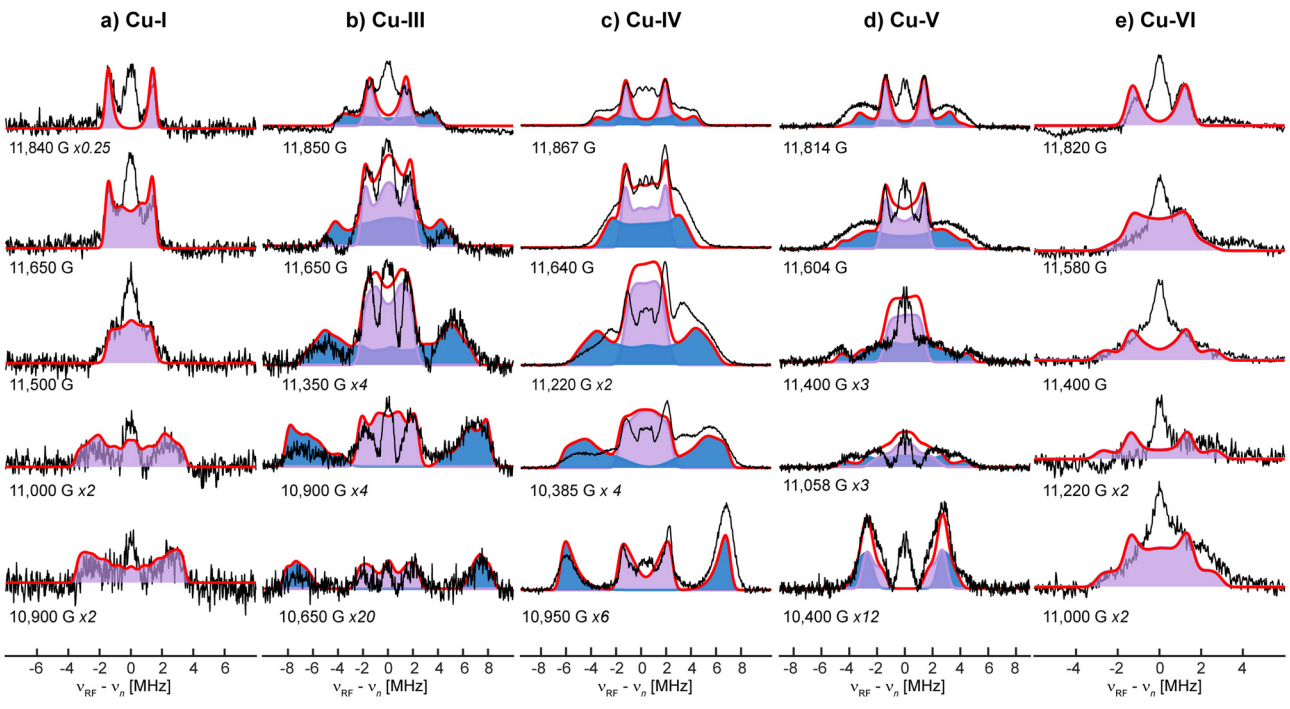

Fig. 3 Q-band (~34.0 GHz) Davies ENDOR responses of the exchangeable protons found in **Cu-I** (a), **Cu-III** (b), **Cu-IV** (c), **Cu-V** (d), and **Cu-VI** (e) in black with simulations in red. The spectra were either recorded through direct measurement (c) or through subtraction of spectra recorded in H_2O and D_2O. Experimental conditions are described in the Experimental section. Simulation parameters are listed in Table 2. The full patterns along with the simulations are displayed in Fig. S17–S21.†

Table 2 ^{1}H hyperfine couplings of the exchangeable protons for copper bpy complexes obtained from simulation

	$\boldsymbol{A}(^1\mathrm{H}) = [A_1, A_2, A_3]$ in MHz	Euler angles[a] $[\alpha, \beta, \gamma]$ in °	a_{iso} in MHz[b]	T in MHz[b]	t in MHz[b]
Cu-I	[+7, −3, −3]	[15, 0, 0]	+0.3	[+6.7, −3.3, −3.3]	+3.3
Cu-III (eq)	[−16.5, −8.0, +7.5]	[0, 0, 0]	−5.6	[−10.9, −2.4, +13.1]	+6.6
Cu-III (ax)	[+4.9, −4.1, −3]	[25, 0, 0]	−0.7	[+5.6, −3.4, −2.3]	+2.8
Cu-IV (eq)	[−13.5, −5, +8.5]	[0, 0, 0]	−3.2	[−10.2, −1.7, +11.8]	+5.9
Cu-IV (ax)	[+4.3, −3.6, −3.4]	[20, 0, 0]	−0.9	[+5.2, −2.7, −2.5]	+2.6
Cu-V (eq)	[−5.5, −9.5, +7.0]	[30, 0, 0]	−2.6	[−2.9, −6.9, +9.6]	+4.9
Cu-V (ax)	[+6, −3, −3;]	[15, 0, 0]	0	[+6, −3, −3]	+3.0
Cu-VI	[+6, −3, −2.8]	[50, 0, 0]	+0.1	[+5.9, −3.1, −2.9]	+3.0

[a] The reported Euler angles describe the angles between the calculated ***g***-tensor and the respective hyperfine tensor and are reported in a zyz' convention. [b] The isotropic and anisotropic components of the hyperfine component a_{iso} and t are calculated as $a_{iso} = \frac{A_1+A_2+A_3}{3}$ and $\boldsymbol{A} = a_{iso} + \boldsymbol{T}$ with $\boldsymbol{T} \approx [-t, -t, 2t]$.

is well reproduced by simulation of a single proton hyperfine tensor ($\boldsymbol{A}^{\mathbf{Cu\text{-}I}}(^1\mathrm{H}) = [+7, -3, -3]$ MHz, Table 2). The small isotropic (a_{iso} = +0.3 MHz) and dipolar couplings (t = +3.3 MHz; $\boldsymbol{T} = \boldsymbol{A} - a_{iso}$; $\boldsymbol{T} = [-t, -t, 2t]$) of this proton are in good agreement with the values observed for the axially coordinating water molecules in other copper complexes and proteins, *e.g.* in the prion protein ($a_{iso} \sim 0$ MHz, $t \sim 2$ MHz)[25] or $[Cu(H_2O)_6]^{2+}$ in $Mg(NH_4)_2(SO_4)_2{\cdot}6H_2O$ (a_{iso} < +0.2 MHz, $t \sim$ +3.7 MHz),[23] reflecting the minimal overlap (Fermi contact) of the axial waters with the $d_{x^2-y^2}$ SOMOs. As is, this signal cannot be exclusively assigned to an equatorially or axially coordinated ligand; however, we will demonstrate experimentally (*vide infra*) that it is indeed from axial H_2O ligand(s), and *no equatorial waters are present*.

While a single exchangeable proton is observed for **Cu-I**, the inclusion of two unique proton signals with very different magnitudes for **Cu-III** and **Cu-IV** is required to reproduce their observed ^{1}H ENDOR pattern. For both samples this includes a proton with larger couplings (**set 1**: $\boldsymbol{A}^{\mathbf{Cu\text{-}III}}(^1\mathrm{H}) = [-16.5, -8.0, +7.5]$ MHz; $\boldsymbol{A}^{\mathbf{Cu\text{-}IV}}(^1\mathrm{H}) = [-13.5, -5.0, +8.5]$ MHz) and another proton of smaller couplings. The latter one is comparable in size to the one presented for **Cu-I** (**set 2**: $\boldsymbol{A}^{\mathbf{Cu\text{-}III}}(^1\mathrm{H}) = [+4.9, -4.1, -3]$ MHz; $\boldsymbol{A}^{\mathbf{Cu\text{-}IV}}(^1\mathrm{H}) = [+4.3, -3.6, -3.4]$ MHz) with small isotropic ($|a_{iso}| \sim \leq 1$ MHz) and also rather small dipolar contributions ($t \sim +3$ MHz), which led us to assign the **set 2** protons to axial H_xO ligands. The shape, however, is less axial and the isotropic component of the hyperfine is larger (Table 2). A possible reason for this is the interaction of solvent waters with the nearby hydroxo ligands, creating a different solvation shell environment compared to the one found for **Cu-I** with water redirected towards the *xy*-plane ($g_\perp$). The potential overlapping signals of axial and second shell waters preclude a detailed assessment of their individual couplings, including the determination of the nature (OH^- and H_2O) of such axial ligands. While we expect the coordination of water ligands to the neutral/negatively charged $[Cu(bpy)(OH)_2]/[Cu(OH)_4]^{2-}$ cores, we cannot conclusively exclude OH^- coordination in the axial positions and will consequently keep referring to those ligands as H_xO. More importantly, the patterns of both **set 1** proton couplings are well resolved yielding tensors exhibiting a considerable amount of rhombic distortion with large anisotropic character that is approximately twice as high as the one found for the axial water in **Cu-I**. Furthermore, a larger isotropic contribution to the hyperfine tensor, a_{iso} = −5.6 MHz (**Cu-III**) and −3.2 MHz (**Cu-IV**), is observed compared to the small +0.3 MHz isotropic coupling of the axial water in **Cu-I**. The increased isotropic character, together with the orientation of t_{max} along $g_\perp$, is consistent with an equatorial ligand that has σ overlap with the $d_{x^2-y^2}$ SOMO, yielding more spin delocalization to the proton *via* Fermi contact interaction. These findings are in excellent agreement with the ^{1}H coupling determined for the hydroxo proton found in the $[Cu(OH)]^+$ unit of zeolites, determined to be [−13.0, −4.5, +11.5] MHz[76], equivalent to an a_{iso} value of −2.0 MHz. The dipolar couplings exhibit an averaged t value of +6.8 MHz, similar to the ones observed for **Cu-III** (+6.6 MHz) and **Cu-IV** (+5.9 MHz), all three with clear deviations from axial symmetry. Therefore, the protons associated with **set 1** are tentatively assigned to equatorially coordinating OH^- ligands. An overview of ^{1}H and ^{17}O couplings in relevant copper studies found in the literature is given in Tables S13 and S14,† respectively.

To further verify the identity of the axially coordinated ligands in the presented complexes, the bis-bpy complex $[Cu(bpy)_2]^{2+}$ (**Cu-VI**) was prepared as described before.[22,41] The steric demands of the ligands force the complex into a pseudo-tetrahedral configuration,[22] precluding equatorial coordination of solvent molecules, allowing additional coordination only in the axial position(s). The ^{1}H ENDOR difference spectra of **Cu-VI** show indeed only a single splitting, which can be simulated with a tensor that is in excellent agreement with the tensor found for **Cu-I** ($\boldsymbol{A}^{\mathbf{Cu\text{-}VI}}(^1\mathrm{H}) = [+6, -3, -2.8]$ MHz; Table 2). This confirms the axial coordination of water in this structure and in **Cu-I**, and also reinforces the assignment of H_xO ligands in the axial position of **Cu-III** and **Cu-IV**. Of note, ENDOR cannot quantify the number of equivalent ligands and can therefore not differentiate between one or two axial H_xO ligands. Similarly, the EPR spectra cannot differentiate between both possibilities.

The resemblance of the exchangeable protons' ^{1}H hyperfine tensors of **Cu-VI** and **Cu-I** strongly suggests that **Cu-I** has no coordinating equatorial waters. One possible reason for this is

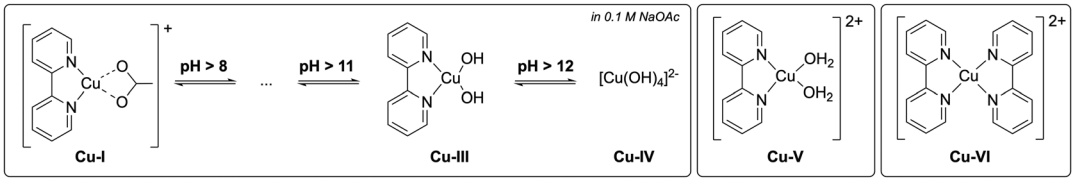

Chart 1 Structures of copper complexes examined in this study. All complexes show resonances of axially coordinating H_xO ligands, which are omitted in the structures for clarity.

the blockage of the equatorial positions through the coordination of the employed sodium acetate at low pH. To test its role, we prepared another 1 : 1 Cu : bpy complex at neutral pH and used glycerol instead of sodium acetate as a glassing agent. A slight shift of the spin Hamiltonian parameters is observed upon change of the glassing agent (Fig. S7†) with an increase of $g_{\|}$ ($|\Delta|$ = 0.032) and a minor decrease of $A_{\|}(^{63}Cu)$ ($|\Delta|$ = 45 MHz) in between **Cu-I** and **Cu-V**, reflecting a change in the coordination sphere. The ^{14}N ENDOR experiments, however, do not exhibit any significant changes, confirming highly similar interactions between the copper center and the bpy ligand, as seen for all bpy complexes (Fig. S22†). The ^{1}H ENDOR difference spectra of **Cu-V** (Fig. 3 and S15†) show two sets of signals. One ^{1}H ENDOR signal of $A \sim 3$ MHz is observed along $g_{\perp}$, strikingly similar to the one observed in **Cu-I**. At this field position, there is also a clear new ^{1}H doublet with a larger observed coupling of 9 MHz. Moving to a lower magnetic field, the ^{1}H ENDOR pattern of **Cu-V** becomes more complex, with large effective splitting still observed halfway through the pattern that collapses into several overlapping signals at the lowest field. This ENDOR pattern is once again satisfactorily reproduced with the inclusion of two different proton hyperfine patterns. Again, a smaller axial coupling (**set 2:** $\boldsymbol{A}^{\mathbf{Cu\text{-}VI}}(^{1}H)$ = [+6, −3, −3] MHz) is observed and assigned to axially coordinating waters. The second set of signals is best simulated with, again, a more rhombic and overall larger tensor of $\boldsymbol{A}^{\mathbf{Cu\text{-}VI}}(^{1}H)$ = [−5.5, −9.5, +7.0] MHz (**set 1**), similar to what has been observed for the equatorial water ligands found in copper bis(oxazoline) ($\boldsymbol{A}(^{1}H)$ = [−10.8, −5.02, +8.6] MHz)[29] and $[Cu(H_2O)_6]^{2+}$ in $Mg(NH_4)_2(SO_4)_2{\cdot}6H_2O$ ($\boldsymbol{A}(^{1}H) \sim$ [+9, −8, −4] MHz, Table S13†).[23] Hence, we attribute the **set 1** proton of **Cu-VI** to equatorial waters. This tensor is still dominated by its anisotropic component (t = +4.9 MHz) but has an appreciable isotropic component, a_{iso} = −2.6 MHz, as expected for an equatorial ligand.

A summary of the resolved exchangeable ^{1}H signals is detailed in Table 2. Overall, smaller isotropic and anisotropic contributions of the hyperfine couplings can be observed for the equatorial ligands in **Cu-V** (a_{iso} = −2.6 MHz; t = +4.9 MHz) compared to **Cu-III** (a_{iso} = −5.6 MHz; t = 6.6 MHz) and **Cu-IV** (a_{iso} = −3.2 MHz; t = +5.9 MHz). This reflects the reduced covalent interaction between the copper center and the H_2O ligand, compared to the OH^- ligand, as seen by the reduction in a_{iso}. Furthermore, the expected increased Cu–O (and thereby Cu–H) distance of $Cu–OH_2$ compared to Cu–OH manifests itself in the smaller value for through-space (distance dependent) anisotropic coupling t. While it is assumed that both **Cu-III** and **Cu-IV** have hydroxo ligands, significant differences can also be observed between the ^{1}H couplings of their exchangeable protons, with overall larger isotropic and anisotropic contributions for **Cu-III**, making **Cu-IV** more similar to **Cu-V** ($|\Delta(a_{iso})|^{\mathbf{IV\text{–}V}}$ = 0.6 MHz; $|\Delta(t)|^{\mathbf{IV\text{–}V}}$ = 1.0 MHz) than to **Cu-III** ($|\Delta(a_{iso})|^{\mathbf{IV\text{–}III}}$ = 2.4 MHz; $|\Delta(t)|^{\mathbf{IV\text{–}III}}$ = 0.7 MHz). This shows that a clear differentiation between H_2O and OH^- ligands by ^{1}H ENDOR alone is not readily feasible. Hence, we further characterized the different H_xO ligands using ^{17}O ENDOR and DFT calculations (see below). An overview of the characterized complexes is given in Chart 1.

^{17}O and ^{14}N ENDOR spectroscopy

Cu-I, **Cu-III**, **Cu-IV**, **Cu-V** and **Cu-VI** were further characterized for their ^{17}O superhyperfine interaction. At the Q-band frequency, ^{17}O resonances of H_xO ligands have the potential to overlap with the ^{14}N resonances of the bpy ligand ($I(^{14}N)$ = 1, 99.6%), both of which fall in the strong coupling regime ($|A| > 2|\nu_n|$) and therefore yield signal pairs centered at $A/2$ split by $2\nu_n$ ($\nu_n(^{14}N) \sim 4$ MHz and $\nu_n(^{17}O) \sim 7$ MHz at 12 000 G). The ^{17}O resonances are distinguished from the overlapping ^{14}N signals of the bpy ligand by overlaying the ENDOR spectra of the ^{17}O labeled and unlabeled samples and subtraction of the two spectra (Fig. 4). The spectra of **Cu-I**, **Cu-III**, **Cu-V** and **Cu-VI** exhibit signal intensities between 15 and 25 MHz (Fig. S23–S27†), which can tentatively be assigned to the ν_+ features of the bpy ligand. The lower frequency feature (ν_-), on the other hand, is cut off due to the lower limit of the employed resonator (as will also be seen for the ^{17}O resonances below). The ^{14}N ENDOR spectra are simulated in conjunction with the respective X-band EPR spectrum of the sample, where both simulations utilize two strongly coupled nitrogen nuclei. For all complexes, the hyperfine tensors of the two nuclei are set to be identical in size, but differ in their orientation, orienting the maximal component of one of the tensors along g_x and the maximal component of the other one along g_y for the approximately square planar complexes. It is important to note that the simulated ^{14}N ENDOR pattern is fairly insensitive to the orientation of the hyperfine tensor in the x and y direction due to their equivalencies in the axial EPR spectrum. While the ENDOR spectrum could be simulated using only one ^{14}N nucleus, the ^{14}N superhyperfine splitting pattern of the EPR spectrum confirms that two equal nuclei are present.

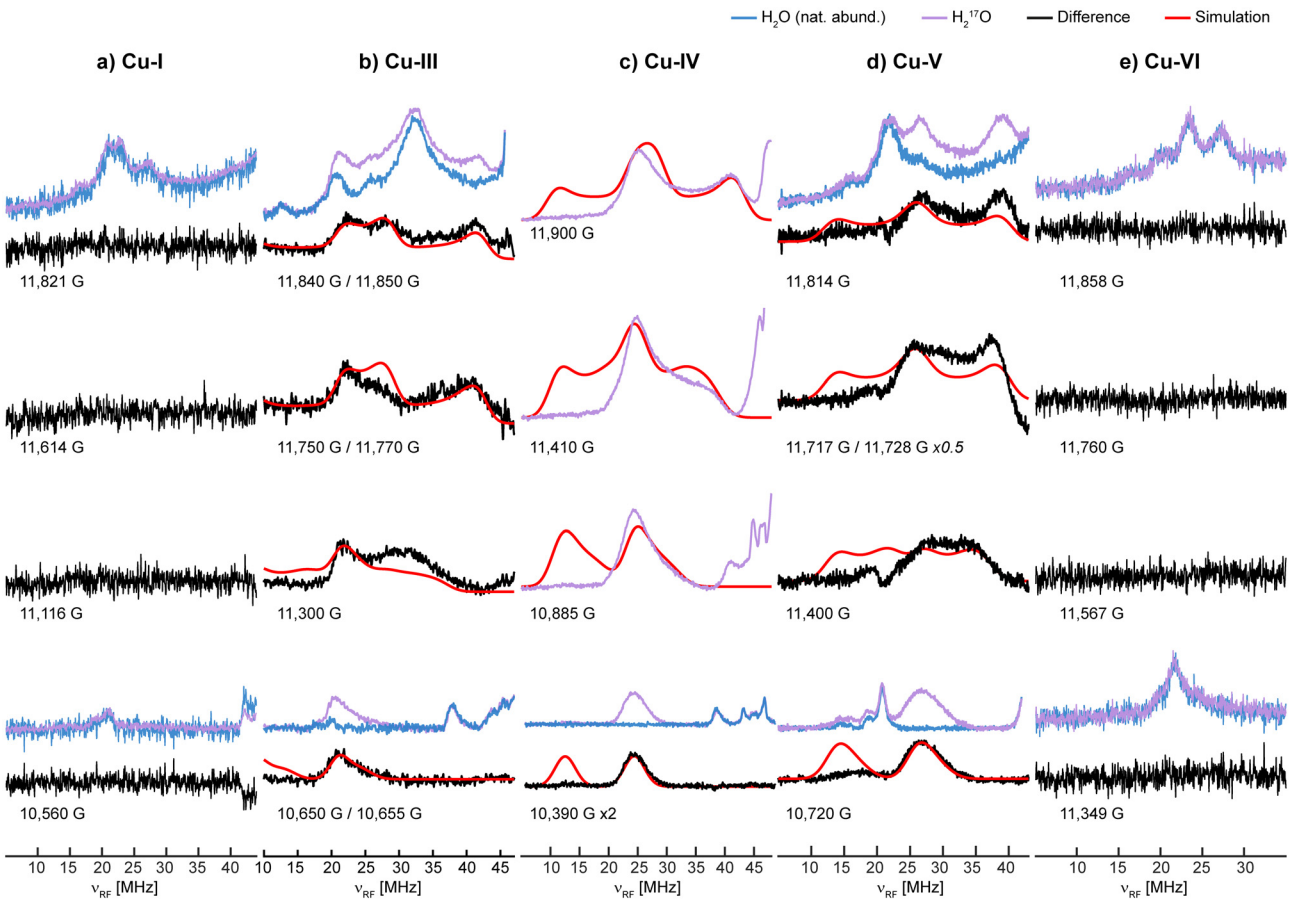

Fig. 4 ^{17}O Q-band (~34.0 GHz) Davies ENDOR responses of **Cu-I** (a), **Cu-III** (b), **Cu-IV** (c), **Cu-V** (d) and **Cu-VI** (e) with simulations in red. The spectra were either recorded through direct measurement (c) or through subtraction (black) of spectra recorded in ^{17}O-enriched H_2O (purple) and H_2O of natural abundance (blue). Experimental conditions are described in the Experimental section. Simulation parameters are listed in Table 3. The full ENDOR patterns together with their simulations are depicted in Fig. S29–S31.†

Comparing the ^{14}N ENDOR spectra of the above-mentioned complexes (Fig. S4, S5, S8 and S9†) shows only negligible differences (Fig. S28†). The patterns can be simulated with mostly isotropic hyperfine tensors of similar sizes and shapes ($\boldsymbol{A}(^{14}N)$ ~ [30, 30, 40] MHz), indicating minimal alterations of the bpy ligand as the pH or the Cu : bpy ratio is varied (Tables S8 and S9†).

Additionally, the ^{14}N ENDOR responses near and at the $g_\perp$ magnetic field positions are further split by 3P due to quadrupole interactions. The axial nature of the $\boldsymbol{g}$-tensor makes the determination of an exact and unique solution to the ^{14}N ENDOR field-frequency pattern rather challenging for copper active sites.[28,77,78] Fig. S4, S5, S8 and S9† show simulations of the data including quadrupole interactions, where the largest component, P_{max}, is aligned along the maximal hyperfine component, which reproduces the peak positions satisfactorily. In fact, the quadrupole tensors agree well with that observed for the imidazole coordination in a lytic polysaccharide monooxygenase, for which a rhombic $\boldsymbol{g}$-tensor allowed for complete orientation selective ENDOR analysis.[28] Ultimately, the size of the nitrogen hyperfine interaction is sufficiently well estimated from the EPR and ENDOR patterns together, which shows no substantial variation among **Cu-I**, **Cu-III**, **Cu-V** and **Cu-VI**. For **Cu-IV**, on the other side, no ^{14}N resonances are observed (Fig. S25†) confirming the loss of the bpy ligand at pH > 12, as already observed by EPR and suggested by ^{1}H ENDOR spectroscopy.

Subsequently, ENDOR spectra of ^{17}O-enriched samples were collected and the spectra of unlabeled samples were subtracted to directly depict the ^{17}O resonances (Fig. S23–S27†). For **Cu-I**, no strongly coupled ^{17}O resonances were observed (Fig. 4), although strong couplings (~30–70 MHz) for equatorial waters are expected.[30,32–34] This ultimately confirms the blockage of the copper center by the added sodium acetate as suggested by the ^{1}H ENDOR experiments above. However, the ^{17}O ENDOR difference spectra of **Cu-V** show clear resonances characteristic of strongly coupled oxygen nuclei (Fig. 4 and S26†). At the 'single crystal-like position', along $g_\parallel$, only a single ν_+ ^{17}O feature is observed at approximately 26.7 MHz. We were unable to detect any ENDOR responses below a radio frequency of ~17 MHz during this experiment, and this lower limit of detection is clearly seen in the ^{14}N responses that fall

off in intensity below this frequency. Because of this limitation of the resonator used, the ν_- feature of the strongly coupled ^{17}O doublet is not observed, nor could weakly coupled ^{17}O interactions near the oxygen Larmor frequency be measured. The observed ν_+ feature at 26.7 MHz corresponds to a coupling of approximately 41.0 MHz. Along $g_\perp$, a ν_+ signal is observed at ~38.7 MHz, with its ν_- feature expected at ~38.7–13.6 = 25.1 MHz as given by $\nu_- = \nu_+ - 2\nu_n$ ($\nu_n(^{17}O)$ = 6.8 MHz at 11 814 G), corresponding to an observed hyperfine coupling of A = 63.8 MHz. However, the feature at ~27 MHz appears broader and with a more asymmetric line shape compared to its ν_+ partner. Therefore, it is suspected that a second ν_+ feature may overlap at this position with a corresponding coupling of approximately A = 40 MHz. This field position is directed along $g_\perp$ and probes both A_2 and A_3 of the ^{17}O hyperfine tensor making the overlap of two different couplings probable. This pattern therefore yields an axial hyperfine tensor for the coordinated ^{17}O nuclei, where the observed pattern is well simulated by a tensor of $\boldsymbol{A}^{\mathbf{Cu\text{-}V}}(^{17}O)$ = [−39, −39, −66] MHz. The signs of all ^{17}O tensors are based on the negative nuclear g_n value of the ^{17}O nucleus and DFT calculations (see below), in agreement with what has been suggested in the literature previously (Table S13†). The simulations shown in Fig. 4 include a second equivalent ^{17}O nucleus whose $\boldsymbol{A}$-tensor is rotated by 90° about the z-axis ($g_\parallel/A_1$) to effectively form $\boldsymbol{A}^{\mathbf{Cu\text{-}V}}(^{17}O)$ = [−39, −66, −39] MHz to account for both directions. However, due to the highly axial nature of the $\boldsymbol{g}$-tensor this inclusion is rather a matter of principle and does not significantly improve the fit, similar to what has been discussed above for the ^{14}N ENDOR simulations. No resolved ^{17}O superhyperfine splitting of the EPR spectra is observed, but only an increased line broadening.

The ^{17}O resonances of **Cu-III** and **Cu-IV** are quite similar in character to **Cu-V**, and can also be simulated with two sets of axial ^{17}O hyperfine tensors, that were set to be identical, but again rotated 90° around the z-axis. **Cu-III** and **Cu-IV** have slightly larger hyperfine couplings than **Cu-V** (Table 3).

Similar to **Cu-I**, no strong ^{17}O resonances were detected for **Cu-VI**, although the ^{1}H ENDOR experiments indicated the coordination of axial water ligands for these and all other studied complexes. In the past, axial water ligands exhibited weak ^{17}O couplings of ~1.5–4 MHz,[4,24,80] with the exception of comparably large couplings of $\boldsymbol{A}$ = [−8, −8, −16] MHz found for copper-exchanged zeolites.[30] However, couplings of this size appear too low for the lower limit of the resonator employed here.

W-band (~94 GHz) ELDOR-detected NMR spectra of **Cu-I**, **Cu-III** and **Cu-IV** were recorded to measure the weakly coupled oxygen nuclei (Fig. S32–S36†). Analogous to the ^{14}N/^{17}O ENDOR experiments, the spectra of ^{17}O-enriched samples were subtracted from the spectra of samples of natural abundance, allowing the creation of difference spectra that only display the ^{17}O resonances (Fig. S37 and S38†). The spectra of **Cu-III** and **Cu-IV** exhibit features of strongly coupled ^{17}O resonances. Simulations with the ^{17}O hyperfine tensors obtained from ENDOR spectroscopy reproduce the EDNMR spectra quite well (Fig. S39 and S40†), further validating the hyperfine tensor estimates from the ENDOR spectroscopy. Additionally, the EDNMR spectra of **Cu-I**, **Cu-III** and **Cu-IV** all exhibit a weakly coupled signal centered at the ^{17}O Larmor frequency ($\nu_n(^{17}O)$ ~ 19 MHz at 33 000 G), indicating the coordination of axial H_xO ligands,[81] and/or other solvent-shell ^{17}O water nuclear interactions. Given the lower resolution of the EDNMR experiment, the data preclude accurate hyperfine estimates for these weak couplings, a known disadvantage of the technique.[81]

The hyperfine tensors of the strongly coupled ^{17}O nuclei in **Cu-III**, **Cu-IV** and **Cu-V** can be divided into their isotropic and dipolar components again, as shown in Table 3. The isotropic components of all three species are in a similar range of −43 to −48 MHz. This is in good agreement with the equatorial water ligands found in copper-exchanged zeolites, with ^{17}O hyperfine couplings between −41 and −51 MHz.[30,32] In the $[Cu(H_2O)_6]^{2+}$ doped Tutton salt two sets of equatorial ligands along g_x and g_y can be differentiated and yield isotropic hyperfine components of −44 and −35 MHz, respectively.[33] The $a_{iso}(^{17}O)$ values of **Cu-III**, **Cu-IV** and **Cu-V** correspond to minimal s orbital spin population (<1%), while the dipolar components of −9 to −14 MHz indicate a considerable amount of p orbital spin density ρ_p, with larger values for the two OH^- coordinated complexes **Cu-III** (t = −14 MHz, ρ_p = 9.4%) and **Cu-IV** (t = −12 MHz, ρ_p = 8.1%), compared to the H_2O-coordinated complex **Cu-V** (t = −9 MHz, ρ_p = 6.1%). The

Table 3 ^{17}O hyperfine couplings of copper bpy complexes obtained from simulation. Other simulation parameters are reported in Table S15†

	$\boldsymbol{A}(^{17}O)$ = [A_1, A_2, A_3] in MHz	a_{iso} in MHz[a]	ρ_s[b] [%]	t in MHz[a,c]	ρ_p[b] [%]
Cu-III	[−29, −72, −29; −29, −29, −72]	−43	0.9	−14	9.4
Cu-IV	[−34, −34, −70; −34, −70, −34]	−46	1.0	−12	8.1
Cu-V	[−39, −66, −39; −39, −39, −66]	−48	1.0	−9	6.1

[a] The isotropic and anisotropic components of the hyperfine tensors, a_{iso} and t, are calculated as follows: $a_{iso} = \frac{A_1 + A_2 + A_3}{3}$ and $\boldsymbol{A} = \boldsymbol{T} + a_{iso}$ with $\boldsymbol{T}$ = [−t, −t, 2t]. The same signs for all three hyperfine components are assumed. [b] s and p orbital spin populations ($\rho_{s,p}$) were estimated from $\rho_s = \frac{a_{iso}}{a_0}$ and $\rho_p = \frac{t}{b_0}$, where a_0 and b_0 are the isotropic and anisotropic hyperfine coupling constants ($a_0(^{17}O)$ = −4622.83 MHz and $b_0(^{17}O)$ = −372.18·2/5 = 148.87 MHz).[79] [c] Based on the DFT calculated Cu–O distances and Mulliken spin populations (**Cu-III**: 1.90 Å; ρ_{Cu} = 0.60 (**DFT-III**); **Cu-IV**: 1.97 Å; ρ_{Cu} = 0.62 (**DFT-IV**); **Cu-V**: 2.02 Å; ρ_{Cu} = 0.67 (**DFT-I**)/2.05 Å; ρ_{Cu} = 0.69 (**DFT-II**)), the non-local contribution to the dipolar hyperfine coupling t is estimated to be only <1 MHz, and therefore neglected in the calculation of p orbital spin density.

dipolar component of the ^{17}O hyperfine tensors of the equatorial waters in copper-exchanged zeolites[30,32] and $[Cu(H_2O)_6]^{2+}$ in the Tutton salt[33] ranges between −6.5 and −9.5 MHz, with the exception of a larger coupling for one of the ^{17}O species in zeolites (t = −12 MHz).[30] While the other couplings are in good agreement with the coupling found for **Cu-V**, the large coupling rather resembles the ^{17}O couplings of the hydroxide ligands in **Cu-III** and **Cu-IV**. The authors discussed the possibility of a hydroxide coordinating instead of water; however, they found the ^{1}H coupling of the respective H_xO ligand to be largely overestimated by DFT (~20 MHz), contradicting their experimental findings. Rather, differences in the hyperfine couplings were attributed to geometrical differences, leading to different degrees of overlap between the Cu $d_{x^2-y^2}$ and the O 2p orbitals. While this may be true for the presented case, we also observe general DFT overestimations of the ^{1}H couplings of hydroxide ligands (see below), suggesting that this may not be an ideal tool to discriminate between the two species.

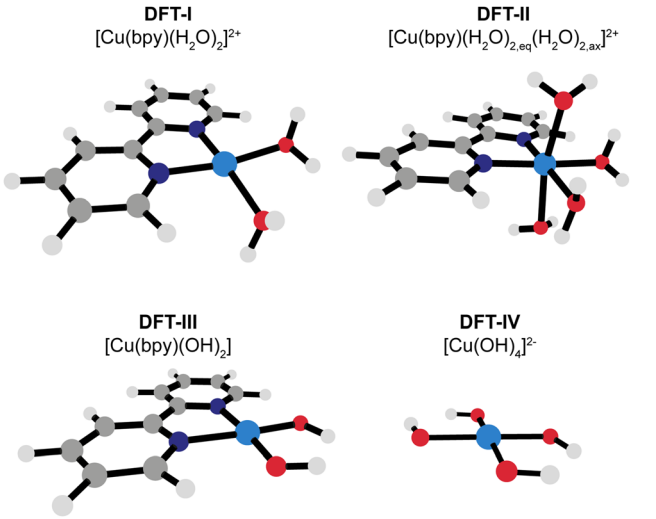

Fig. 5 DFT-optimized structures of **DFT-I**, **DFT-II**, **DFT-III** and **DFT-IV**. Cu: light blue, O: red, N: dark blue, C: dark gray, and H: light gray.

DFT calculations

To shed further light on the speciation of copper bpy complexes depending on pH, DFT calculations on $[Cu(bpy)(H_2O)_2]^{2+}$ (**DFT-I**), $[Cu(bpy)(OH)_2]$ (**DFT-III**) and $[Cu(OH)_4]^{2-}$ (**DFT-IV**) were carried out, as well as on the corresponding complexes with additional axial water molecules ($[Cu(bpy)(H_2O)_{2,eq}(H_2O)_{2,ax}]^{2+}$ (**DFT-II**), $[Cu(bpy)(OH)_{2,eq}(H_2O)_{2,ax}]$ (**DFT-V**) and $[Cu(OH)_{4,eq}(H_2O)_{2,ax}]^{2-}$ (**DFT-VI**)). The DFT calculated spin Hamiltonian parameters of all examined complexes are listed in Tables 4 and S16.† The geometry optimizations of **DFT-V** and **DFT-VI** yielded structures without the axial water molecules, caused by their interaction with the hydroxyl ions nearby and the lack of an explicit solvation model. Therefore, these complexes are not further discussed below. The optimized structures of **DFT-I**, **DFT-II**, **DFT-III** and **DFT-IV** are depicted in Fig. 5.

As expected, the DFT calculations yielded fairly axial $\boldsymbol{g}$- and $\boldsymbol{A}(^{63}Cu)$-tensors with $g_\parallel > g_\perp$ and $A_\parallel \gg A_\perp$ for all examined complexes (Table S16†). For the water coordinated structures slightly higher $g_\parallel$ and negligibly lower $A_\parallel$ values are observed when considering axial water molecules (**DFT-II**) compared to the structure with equatorial waters only (**DFT-I**) due to the slightly larger induced ligand field. Overall, the calculated g-shift trends of $g_\parallel$(**DFT-I**, **DFT-II**) > $g_\parallel$(**DFT-IV**) > $g_\parallel$(**DFT-III**) are in good agreement with the experimental observations ($g_\parallel$(**Cu-V**) > $g_\parallel$(**Cu-IV**) > $g_\parallel$(**Cu-III**)). The changes in $A_\parallel$ are rather small in the experimental and calculated values. However, the calculations do reproduce the slightly smaller $A_\parallel$ value of **Cu-V** (**DFT-I**, **DFT-II**) compared to the two hydroxo complexes.

The DFT calculated ^{1}H and ^{17}O ligand hyperfine couplings are in relatively good agreement with the experimentally determined values and trends observed (Table 4). The axial water molecules in **DFT-II** have rather small, axial ^{1}H hyperfine interactions of $\boldsymbol{A}(^{1}H)$ ~ [+6, −3, −3] MHz and ^{17}O couplings of 1–3 MHz, which reproduces the experimental observations of all examined complexes quite well, further supporting the observation of the axially coordinated water by ^{1}H ENDOR and ^{17}O EDNMR spectroscopy, respectively.

For the equatorial water couplings in **DFT-I** and **DFT-II**, larger, rhombic ^{1}H couplings are calculated, as seen in the ^{1}H ENDOR experiments above. The corresponding ^{17}O hyperfine tensors have isotropic components of −40 to −46 MHz and dipolar couplings of $t(^{17}O)$ ~ −9 MHz. For the two hydroxo complexes **DFT-III** and **DFT-IV** $a_{iso}(^{17}O)$ is found to be in the same range. Their dipolar components, however, are calculated to be significantly higher with $t(^{17}O)$ ~ −20 MHz for

Table 4 Representative[a], calculated ligand hyperfine interactions and the respective Mulliken spin densities of copper bpy complexes

	Ligand hyperfine interactions in MHz				Spin populations ρ		
	$\boldsymbol{A}(^{1}H) = [A_1, A_2, A_3]$	$\boldsymbol{A}(^{17}O) = [A_1, A_2, A_3]$	$a_{iso}(^{17}O)$	$t(^{17}O)$	Cu	Sum(O)	Sum(N)
DFT-I	[−7.7, +9.0, −3.1]	[−34, −61, −35]	−43/−46	−9	0.67	0.10	0.23
DFT-II (eq.)	[−8.0, +8.2, −3.9]	[−32, −32, −59]	−41/−40	−8/−9	0.69	0.09	0.22
DFT-II (ax.)	[+5.7, −2.8, −2.7]	[1.0, 2.5, 2.4]	2.0/2.2	−0.5			
DFT-III	[−22.3, −10.8, +7.4]	[−20, −81, −20]	−40	−20	0.60	0.26	0.14
DFT-IV	[−16.4, −7.2, +7.8]	[−30, −73, −29]	−44/−43	−14/−15	0.62	0.36	[—]

[a] The hyperfine interactions of the individual ligands vary slightly. For clarity, one coupling per ligand is listed. All tensors are listed in Table S16.†

DFT-III and $t(^{17}O) \sim -14$ MHz for **DFT-IV**. This is a significant overestimation compared to their experimental values (**Cu-III**: $t(^{17}O) \sim -14$ MHz; **Cu-IV**: $t(^{17}O) \sim -12$ MHz), especially for **DFT-III**. While the shape of the corresponding ^{1}H couplings of the hydroxo ligands is overall quite well reproduced, the couplings are again overestimated ($\boldsymbol{A}^{\mathbf{DFT\text{-}III}}(^{1}H) = [-22.3, -10.8, +7.4]$ MHz, $\boldsymbol{A}^{\mathbf{DFT\text{-}IV}}(^{1}H) \sim [-16.4, -7.2, +7.8]$ MHz) compared to the experimental values of **Cu-III** ($[-16.5, -8.0, +7.5]$ MHz) and **Cu-IV** ($[-13.0, -5.0, +8.5]$ MHz).

Differences between the hyperfine spectroscopic footprints of the individual complexes can be explained by changes in the spin densities of the ligands. The DFT-calculated Mulliken spin populations of all complexes are listed in Table 4. Between **DFT-I** and **DFT-II** the spin populations on the oxygen ($\rho_{sum}(^{17}O) \sim 0.1/0.09$) and also nitrogen ($\rho_{sum}(^{14}N) \sim 0.22/0.23$) nuclei stay constant, as the additional axial water molecules do not bear a significant amount of spin themselves or significantly influence the existing spin distribution on the rest of the complex. However, as the bis-aqua complex is converted into the bis-hydroxo complex (**DFT-III**), significantly more spin density is found on the OH^- ligands ($\rho_{sum}(^{17}O) \sim 0.26$), while the contrary observation can be made for the bpy ligand ($\rho_{sum}(^{14}N) \sim 0.14$). This leads to a larger anisotropic hyperfine interaction for the ^{17}O nuclei for **DFT-III** ($t \sim -20$ MHz) compared to **DFT-I** ($t \sim -9$ MHz). The effects of the OH^- ligands in **DFT-III** slightly outweigh the effects of the bpy ligand, leading to an overall reduced spin density on the copper center (**DFT-I**: 0.67; **DFT-III**: 0.60). The tetra-hydroxo model **DFT-IV** bears approximately the same spin population on the copper center (0.62), and also on the ligands. However, the distribution of the spin density over four instead of two OH^- ligands significantly reduces the density per ligand, and thereby also the hyperfine coupling ($t \sim -14/-15$ MHz).

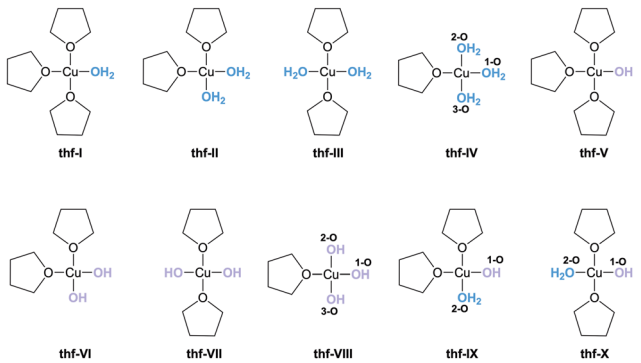

Chart 2 Overview of the DFT calculated structures **thf-I–thf-X**.

The relatively large difference in the ^{17}O ligand hyperfine couplings between **Cu-III** and **Cu-IV** inspired us to further explore the variability of this property, including the effects of ligand charge. Hence, we optimized the geometries of several square planar copper complexes with the neutral tetrahydrofuran (thf) ligand in various thf : H_xO ratios (complexes **thf-I–thf-X**, shown in Chart 2). The aquo complexes **thf-I–thf-IV** with $n = 1$ to 3 water and 4-n thf molecules exhibit highly similar ^{17}O hyperfine couplings with isotropic components between -47 and -49 MHz and anisotropic components ranging between -10 and -11 MHz (Table 5). For the hydroxo complexes **thf-V–thf-VIII**, on the other hand, significant variations in the ^{17}O hyperfine are observed with a_{iso} values between -18 and -51 MHz and t values between -10 and -25 MHz. It is noticeable that the ^{17}O couplings of OH^- ligands, that have a second OH^- ligand in *trans* position exhibit significantly smaller anisotropic hyperfine components ($t \sim -10$ to -12 MHz), approximately half of the couplings found for OH^- ligands positioned *trans* to a thf ligand ($t \sim -21$ to -25 MHz).

The mixed H_2O/OH^- complexes **thf-IX** and **thf-X** with two thf molecules and the H_xO ligands either in *cis* (**thf-IX**) or *trans* (**thf-X**) positions to each other (Chart 2) were examined as well.

Table 5 Calculated ^{17}O hyperfine couplings of the H_xO ligands in complexes **thf-I–thf-X**, together with the optimized Cu–O bond distances

	$\boldsymbol{A} = [A_1, A_2, A_3]$ in MHz	a_{iso} in MHz	t in MHz	Cu–O distance in Å	Mulliken spin density
thf-I	[−37, −67, −36]	−47	−10	1.991	0.06
thf-II	[−38, −69, −38]	−49	−10	1.997	0.06
	[−68, −36, −36]	−47	−10	1.998	0.06
thf-III	[−36, −68, −35]	−47	−11	1.985	0.06
	[−36, −68, −35]	−47	−11	1.988	0.06
thf-IV	**1-O:** [−68, −36, −37]	**1-O:** −48	**1-O:** −10	1.986	0.06
	2-O: [−35, −71, −35]	**2-O:** −48	**2-O:** −11	1.986	0.07
	3-O: [−39, −69, −37]	**3-O:** −49	**3-O:** −10	1.983	0.06
thf-V	[−71, −5, −3]	−28	−21	1.847	0.15
thf-VI	[−8, −76, −9]	−32	−22	1.876	0.15
	[−10, −81, −10]	−35	−23	1.882	0.15
thf-VII	[−41, −4, −5]	−18	−12	1.859	0.08
	[−41, −4, −5]	−18	−12	1.859	0.08
thf-VIII	**1-O:** [−23, −102, −24]	**1-O:** −51	**1-O:** −25	1.940	0.16
	2-O: [−52, −19, −20]	**2-O:** −32	**2-O:** −10	1.896	0.07
	3-O: [−51, −18, −18]	**3-O:** −30	**3-O:** −10	1.891	0.07
thf-IX	**1-O:** [−68, −1, 0]	**1-O:** −26	**1-O:** −21	1.843	0.15
	2-O: [−51, −83, −52]	**2-O:** −62	**2-O:** −10	2.045	0.05
thf-X	**1-O:** [−73, −3, −5]	**1-O:** −29	**1-O:** −22	1.842	0.15
	2-O: [−41, −22, −23]	**2-O:** −29	**2-O:** −6	2.017	0.03

The OH^- ligands of **thf-IX** and **thf-X** show comparable hyperfine couplings to the ones determined for the *trans*-thf positioned OH^- couplings in **thf-V–thf-VIII**. The ^{17}O coupling of the H_2O ligand in **thf-IX** also exhibits couplings comparable to the ones found for **thf-I–thf-IV**. In **thf-X**, however, where the H_2O ligand is positioned *trans* to the OH^- ligand, the isotropic and anisotropic components are again approximately halved compared to the one found in **thf-IX**. This again indicates that the OH^- ligand has a major influence on ligands that are *trans*-positioned, as their spin density is approximately halved (Table 5).

A potential reason for variations in the hyperfine couplings is the distortion from an ideal square planar geometry, leading to a reduced overlap of the O 2p orbitals with the $d_{x^2-y^2}$ SOMO. To examine this influence, the optimized structure of **DFT-IV** was stepwise distorted by simultaneously constraining the O1–Cu–O2 and O3–Cu–O4 ($O–Cu–O^{cis}$) angles from 90° to 109.5° and reoptimizing the rest of the structure (Fig. S41a†). The subsequently calculated ^{17}O hyperfine couplings are listed in Table S17,† showing only minor changes in t, while a_{iso} is reduced from −44 MHz ($O–Cu–O^{cis}$: 90°, $O–Cu–O^{trans}$: 133°) to −25 MHz ($O–Cu–O^{cis}$: 109.5°, $O–Cu–O^{trans}$: 133°) (Fig. S41b†). This can in part be the reason for variations in the isotropic ^{17}O couplings of **thf-I–thf-X**; however, the observed distortions in these complexes are rather small with $O–Cu–O^{trans}$ angles of between 169° and 179°, suggesting that distortions from square planar have only minor effects on hyperfine couplings. In particular, the minimal influence of the distortion on t shows, that the ^{17}O hyperfine variations found in **thf-I–thf-X** are better explained by the electronic effects of *trans* positioned hydroxide than geometry distortions.

Altogether, we conclude that the spectroscopic "footprints" of H_xO ligands do not only depend on their inherent nature (OH^- *vs.* H_2O), but are also heavily influenced by other ligands *trans* to them, with a clear reduction of its anisotropic components when the *trans* positioned ligand is another hydroxo ligand.

Conclusion

The ability to accurately identify the coordination sphere of a catalytic metal center is essential for understanding and assigning mechanisms. Advanced EPR techniques, such as ENDOR and EDNMR spectroscopy (both employed here) and other hyperfine approaches such as electron stimulated echo envelope modulation (ESEEM) and hyperfine sublevel correlation (HYSCORE) spectroscopy have unique abilities to characterize frozen, randomly oriented (powder like) paramagnetic catalytic centers with high resolution. The extraction of structural information and accurate ligand identification requires both clear standards and an understanding of various influential factors of hyperfine couplings.

We have examined aqueous copper bpy solutions between pH 7 and pH 14 by employing UV-Vis and EPR spectroscopy. In solutions with added sodium acetate, $[Cu(bpy)(OAc)(H_2O)_{2,ax}]^+$ (**Cu-I**) forms at neutral pH and no waters coordinate in the equatorial positions. Using glycerol instead of sodium acetate as a glassing agent for EPR spectroscopy generates the acetate-free $[Cu(bpy)(H_2O)_{2,eq}(H_2O)_{2,ax}]^{2+}$ (**Cu-V**). This in part demonstrates the powerful ability of EPR and advanced EPR spectroscopy to confirm the coordination environment of a catalytic center under conditions used in catalysis. At pH 12, the signal is completely recovered and the only detectable species is the bis-hydroxo complex $[Cu(bpy)(OH)_{2,eq}(H_xO)_{2,ax}]$ (**Cu-III**). At even further elevated pH, the complex loses the bpy ligand and the tetra-hydroxo complex $[Cu(OH)_{4,eq}(H_xO)_{2,ax}]^{2-}$ (**Cu-IV**) emerges.

^1H and ^{17}O ENDOR spectra of the various copper complexes studied here reveal both clear trends and ambiguity in the differentiation of equatorial *vs.* axial waters, and differentiation difficulties between water and hydroxo ligands. The equatorial H_xO ligand shows relatively large and rhombic ^1H couplings, whereas the couplings are generally larger for the OH^- compared to the H_2O ligands. Their ^{17}O nuclei exhibit axial hyperfine couplings, with the maximum hyperfine interaction directed along the Cu–O bonds. Analogous to the proton couplings, the ^{17}O nuclei of the hydroxo ligands in **Cu-III** and **Cu-IV** exhibit larger dipolar couplings than the coordinating water molecules in **Cu-V**. Additionally, in between **Cu-III** and **Cu-IV** the ^1H and ^{17}O couplings show clear differences, with generally larger couplings for **Cu-III**. We showed computationally that the *trans* positioned ligand heavily influences the anisotropic component of the ^{17}O hyperfine couplings with a clear reduction in $t(^{17}O)$ when a OH^- is at the *trans* position. The observations and influences identified here are generally applicable to the study of copper WOC systems by EPR spectroscopy, but also more broadly to other monocopper active sites, such as LPMOs, where the *trans* coordinating N-terminal amino group ligand is thought to tune reactivity.

Author contributions

JH performed all EPR, ENDOR, EDNMR and UV-Vis experiments and analysis under the supervision of GEC. JH wrote the original draft with contributions from GEC. GEC conceptualized the experiments. GEC acquired funding.

Data availability

All data supporting the findings and conclusions are available in the ESI.†

Conflicts of interest

There are no conflicts of interest to declare.

Acknowledgements

The Max Planck Society is acknowledged for generous financial support.

References

1 J. P. Klinman, The Copper-Enzyme Family of Dopamine β-Monooxygenase and Peptidylglycine α-Hydroxylating Monooxygenase: Resolving the Chemical Pathway for Substrate Hydroxylation, *J. Biol. Chem.*, 2006, **281**(6), 3013–3016, DOI: **10.1074/jbc.r500011200**.

2 G. Vaaje-Kolstad, B. Westereng, S. J. Horn, Z. Liu, H. Zhai, M. Sørlie and V. G. H. Eijsink, An Oxidative Enzyme Boosting the Enzymatic Conversion of Recalcitrant Polysaccharides, *Science*, 2010, **330**(6001), 219–222, DOI: **10.1126/science.1192231**.

3 R. J. Quinlan, M. D. Sweeney, L. Lo Leggio, H. Otten, J. C. N. Poulsen, K. S. Johansen, K. B. R. M. Krogh, C. I. Jørgensen, M. Tovborg, A. Anthonsen, T. Tryfona, C. P. Walter, P. Dupree, F. Xu, G. J. Davies and P. H. Walton, Insights into the Oxidative Degradation of Cellulose by a Copper Metalloenzyme That Exploits Biomass Components, *Proc. Natl. Acad. Sci. U. S. A.*, 2011, **108**(37), 15079–15084, DOI: **10.1073/pnas.1105776108**.

4 M. O. Ross, F. MacMillan, J. Wang, A. Nisthal, T. J. Lawton, B. D. Olafson, S. L. Mayo, A. C. Rosenzweig and B. M. Hoffman, Particulate Methane Monooxygenase Contains Only Mononuclear Copper Centers, *Science*, 2019, **364**(6440), 566–570, DOI: **10.2210/pdb3rgb/pdb**.

5 A. E. Wendlandt, A. M. Suess and S. S. Stahl, Copper-Catalyzed Aerobic Oxidative C-H Functionalizations: Trends and Mechanistic Insights, *Angew. Chem., Int. Ed.*, 2011, **50**(47), 11062–11087, DOI: **10.1002/anie.201103945**.

6 P. Vanelderen, J. Vancauwenbergh, B. F. Sels and R. A. Schoonheydt, Coordination Chemistry and Reactivity of Copper in Zeolites, *Coord. Chem. Rev.*, 2013, **257**(2), 483–494, DOI: **10.1016/j.ccr.2012.07.008**.

7 J. Aguila-Rosas, D. Ramos, C. T. Quirino-Barreda, J. A. Flores-Aguilar, J. L. Obeso, A. Guzmán-Vargas, I. A. Ibarra and E. Lima, Copper(II)-MOFs for Bio-Applications, *Chem. Commun.*, 2023, **59**(79), 11753–11766, DOI: **10.1039/d3cc03146b**.

8 X. Gao, H. Wang and J. Wang, Functional Metal-Organic Framework – a Review of Research on Cu-MOFs, *J. Coord. Chem.*, 2024, **77**, 1307–1323, DOI: **10.1080/00958972.2024.2374881**.

9 H. Lee, X. Wu and L. Sun, Copper-Based Homogeneous and Heterogeneous Catalysts for Electrochemical Water Oxidation, *Nanoscale*, 2020, **12**(7), 4187–4218, DOI: **10.1039/c9nr10437b**.

10 S. M. Barnett, K. I. Goldberg and J. M. Mayer, A Soluble Copper-Bipyridine Water-Oxidation Electrocatalyst, *Nat. Chem.*, 2012, **4**(6), 498–502, DOI: **10.1038/nchem.1350**.

11 M. K. Coggins, M. T. Zhang, Z. Chen, N. Song and T. J. Meyer, Single-Site Copper(II) Water Oxidation Electrocatalysis: Rate Enhancements with HPO42- as a Proton Acceptor at PH 8, *Angew. Chem., Int. Ed.*, 2014, **53**(45), 12226–12230, DOI: **10.1002/anie.201407131**.

12 F. Chen, N. Wang, H. Lei, D. Guo, H. Liu, Z. Zhang, W. Zhang, W. Lai and R. Cao, Electrocatalytic Water Oxidation by a Water-Soluble Copper(II) Complex with a Copper-Bound Carbonate Group Acting as a Potential Proton Shuttle, *Inorg. Chem.*, 2017, **56**(21), 13368–13375, DOI: **10.1021/acs.inorgchem.7b02125**.

13 T. Zhang, C. Wang, S. Liu, J.-L. Wang and W. Lin, A Biomimetic Copper Water Oxidation Catalyst with Low Overpotential, *J. Am. Chem. Soc.*, 2014, **136**(1), 273–281, DOI: **10.1021/ja409267p**.

14 L. Z. Fu, T. Fang, L. L. Zhou and S. Z. Zhan, A Mononuclear Copper Electrocatalyst for Both Water Reduction and Oxidation, *RSC Adv.*, 2014, **4**(96), 53674–53680, DOI: **10.1039/c4ra07211a**.

15 M. Gil-Sepulcre, P. Garrido-Barros, J. Oldengott, I. Funes-Ardoiz, R. Bofill, X. Sala, J. Benet-Buchholz and A. Llobet, Consecutive Ligand–based Electron Transfer in New Molecular Cu–based Water Oxidation Catalysts, *Angew. Chem., Int. Ed.*, 2021, **60**, 18639–18644, DOI: **10.1002/anie.202104020**.

16 S. J. Koepke, K. M. Light, P. E. Vannatta, K. M. Wiley and M. T. Kieber-Emmons, Electrocatalytic Water Oxidation by a Homogeneous Copper Catalyst Disfavors Single-Site Mechanisms, *J. Am. Chem. Soc.*, 2017, **139**(25), 8586–8600, DOI: **10.1021/JACS.7B03278**.

17 D. L. Gerlach, S. Bhagan, A. A. Cruce, D. B. Burks, I. Nieto, H. T. Truong, S. P. Kelley, C. J. Herbst-Gervasoni, K. L. Jernigan, M. K. Bowman, S. Pan, M. Zeller and E. T. Papish, Studies of the Pathways Open to Copper Water Oxidation Catalysts Containing Proximal Hydroxy Groups during Basic Electrocatalysis, *Inorg. Chem.*, 2014, **53**(24), 12689–12698, DOI: **10.1021/ic501018a**.

18 P. Garrido-Barros, I. Funes-Ardoiz, S. Drouet, J. Benet-Buchholz, F. Maseras and A. Llobet, Redox Non-Innocent Ligand Controls Water Oxidation Overpotential in a New Family of Mononuclear Cu-Based Efficient Catalysts, *J. Am. Chem. Soc.*, 2015, **137**(21), 6758–6761, DOI: **10.1021/jacs.5b03977**.

19 Q.-Y. Mao, Y.-J. Pang, X.-C. Li, G.-J. Chen and H.-W. Tan, Theoretical Study of the Mechanisms of Two Copper Water Oxidation Electrocatalysts with Bipyridine Ligands, *ACS Catal.*, 2019, **9**, 8798–8809, DOI: **10.1021/acscatal.9b01022**.

20 M. S. Ali Akbari, S. Nandy, K. H. Chae, R. Bikas, A. Kozakiewicz-Piekarz and M. M. Najafpour, Water Oxidation by a Copper(II) Complex with 6,6′-Dihydroxy-2,2′-Bipyridine Ligand: Challenges and an Alternative Mechanism, *Langmuir*, 2023, **39**(15), 5542–5553, DOI: **10.1021/acs.langmuir.3c00322**.

21 T. Ghosh, P. Ghosh and G. Maayan, A Copper-Peptoid as a Highly Stable, Efficient, and Reusable Homogeneous Water

Oxidation Electrocatalyst, *ACS Catal.*, 2018, **8**(11), 10631–10640, DOI: 10.1021/acscatal.8b03661.

22 E. Garribba, G. Micera, D. Sanna and L. Strinna-Erre, The Cu(II)-2,2-Bipyridine System Revisited, *Inorg. Chim. Acta*, 2000, **299**, 253–261, DOI: 10.1016/s0020-1693(99)00508-3.

23 N. M. Atherton and A. J. Horsewill, Proton ENDOR of Cu$(H_2O)_6^{2+}$ in $Mg(NH_4)_2(SO_2)_4{\cdot}6H_2O$, *Mol. Phys.*, 1979, **37**(5), 1349–1361, DOI: 10.1080/00268977900100991.

24 D. Kim, N. H. Kim and S. H. Kim, 34 GHz Pulsed ENDOR Characterization of the Copper Coordination of an Amyloid β Peptide Relevant to Alzheimer's Disease, *Angew. Chem., Int. Ed.*, 2013, **52**(4), 1139–1142, DOI: 10.1002/anie.201208108.

25 C. S. Burns, E. Aronoff-Spencer, C. M. Dunham, P. Lario, N. I. Avdievich, W. E. Antholine, M. M. Olmstead, A. Vrielink, G. J. Gerfen, J. Peisach, W. G. Scott and G. L. Millhauser, Molecular Features of the Copper Binding Sites in the Octarepeat Domain of the Prion Protein, *Biochemistry*, 2002, **41**(12), 3991–4001, DOI: 10.1021/bi011922x.

26 A. Pöppl and L. Kevan, A Practical Strategy for Determination of Proton Hyperfine Interaction Parameters in Paramagnetic Transition Metal Ion Complexes by Two-Dimensional HYSCORE Electron Spin Resonance Spectroscopy in Disordered Systems, *J. Phys. Chem.*, 1996, **100**(9), 3387–3394, DOI: 10.1021/jp9525999.

27 R. J. Jodts, M. O. Ross, C. W. Koo, P. E. Doan, A. C. Rosenzweig and B. M. Hoffman, Coordination of the Copper Centers in Particulate Methane Monooxygenase: Comparison between Methanotrophs and Characterization of the CuC Site by EPR and ENDOR Spectroscopies, *J. Am. Chem. Soc.*, 2021, **143**(37), 15358–15368, DOI: 10.1021/jacs.1c07018.

28 J. Haak, O. Golten, M. Sørlie, V. Eijsink and G. Cutsail III, pH-Mediated Manipulation of the Histidine Brace in LPMOs and Generation of a Tri-Anionic Variant, Investigated by EPR, ENDOR, ESEEM and HYSCORE Spectroscopy, *Chem. Sci.*, 2024, DOI: 10.1039/d4sc04794j.

29 M. E. Owen, E. Carter, G. J. Hutchings, B. D. Ward and D. M. Murphy, Influence of Counterions on the Structure of Bis(Oxazoline)Copper(II) Complexes; an EPR and ENDOR Investigation, *Dalton Trans.*, 2012, **41**(36), 11085–11092, DOI: 10.1039/c2dt31273e.

30 P. C. Bruzzese, E. Salvadori, S. Jäger, M. Hartmann, B. Civalleri, A. Pöppl and M. Chiesa, ^{17}O-EPR Determination of the Structure and Dynamics of Copper Single-Metal Sites in Zeolites, *Nat. Commun.*, 2021, **12**(1), 4638, DOI: 10.1038/s41467-021-24935-7.

31 Y. K. Liao, P. C. Bruzzese, E. Salvadori and M. Chiesa, ^{17}O Hyperfine Spectroscopy in Surface Chemistry and Catalysis, *J. Magn. Reson. Open*, 2023, **16–17**, 100101, DOI: 10.1016/J.JMRO.2023.100101.

32 A. Actis, E. Salvadori and M. Chiesa, Framework Coordination of Single-Ion Cu^{2+} Sites in Hydrated ^{17}O-ZSM-5 Zeolite, *Catal. Sci. Technol.*, 2021, **11**(15), 5191–5199, DOI: 10.1039/d1cy00838b.

33 D. Getz and B. L. Silver, ESR of $Cu^{2+}(H_2O)_6$. I. The Oxygen-17 Superhyperfine Tensors in $^{63}Cu^{2+}$ Doped Zinc Tutton's Salt at 20°K, *J. Chem. Phys.*, 1974, **61**(2), 630–637, DOI: 10.1063/1.1681939.

34 B. L. Silver, D. Getz and Z. Luz, ^{17}O Superhyperfine Interaction in the ESR Spectrum of Hydrated Cu^{2+} Ion, *Chem. Phys. Lett.*, 1972, **13**(2), 113–114, DOI: 10.1016/s0009-2614(72)90001-2.

35 T. Wagner-Jauregg, B. E. Hackley, J. T. A. Lies, O. O. Owens and R. Proper, Model Reactions of Phosphorous-Containing Enzyme Inactivators. IV. The Catalytic Activity of Certain Metal Salts and Chelates in the Hydrolysis of Diisopropyl Fluorophosphate, *J. Am. Chem. Soc.*, 1955, **77**(4), 922–929, DOI: 10.1021/ja01609a037.

36 A. E. Martell, S. Chaberek, J. R. C. Courtney, S. Westerback and H. Hyytiainen, Hydrolytic Tendencies of Metal Chelate Compounds. I. Cu(II) Chelates, *J. Am. Chem. Soc.*, 1957, **45**, 3036–3041, DOI: 10.1021/ja01512a005.

37 L. B. Ryland, G. S. Ronay and F. M. Fowkes, Equilibria in Aqueous Solutions of Copper(II) Chelates with Alpha, Alpha'-Dipyridyl, o-Phenanthroline and Ethylenediamine, *J. Phys. Chem.*, 1958, **62**, 798–801, DOI: 10.1021/j150565a006.

38 R. L. Gustafson and A. E. Martell, Hydrolytic Tendencies of Metal Chelate Compounds. V. Hydrolysis and Dimerization of Copper(II) Chelates of 1,2-Diamines, *J. Am. Chem. Soc.*, 1959, **81**(3), 525–529, DOI: 10.1021/ja01512a005.

39 D. D. Perrin and V. S. Sharma, Complex Formation by Hydrolysed Copper(II) Ions in Aqueous Solution, *J. Inorg. Nucl. Chem.*, 1966, **28**, 1271–1278, DOI: 10.1016/0022-1902(66)80454-2.

40 M. Noack and G. Gordon, Oxygen-17 NMR and Copper EPR Linewidths in Aqueous Solutions of Copper(II) Ion and 2,2′-Dipyridine, *J. Chem. Phys.*, 1968, **48**(6), 2689–2699, DOI: 10.1063/1.1669503.

41 F. A. Walker, H. Sigel and D. B. McCormick, Spectral Properties of Mixed-Ligand Copper(II) Complexes and Their Corresponding Binary Parent Complexes, *Inorg. Chem.*, 1972, **11**(11), 2756–2763, DOI: 10.1021/ic50117a036.

42 H. Sigel, What Is the Reason for the Cis Configuration of Diaquo-Cu^{2+}-$(2,2'\text{-Bipyridyl})_2$ in Aqueous Solution?, *Inorg. Chim. Acta*, 1972, **6**(2), 195, DOI: 10.1016/s0020-1693(00)91785-7.

43 G. Arena, R. Calì, E. Rizzarelli and S. Sammartano, Thermodynamics of Copper(II) 2,2′-Dipyridyl Complexes in Aqueous Solution, *Thermochim. Acta*, 1976, **17**(2), 155–164, DOI: 10.1016/0040-6031(76)85022-8.

44 I. N. Marov, V. K. Belyaeva, E. B. Smirnova and I. F. Dolmanova, Electron Spin Resonance Spectra of Copper(II) Bipyridyl Complexes, *Inorg. Chem.*, 1978, **17**(6), 1667–1669, DOI: 10.1021/ic50184a058.

45 L. Banci, A. Bencini, D. Gatteschi and C. Zanchini, EPR Spectra of Triplet States with Large Zero-Field Splitting. $[Cu(Bipy)(OH)]_2SO_4{\cdot}4H_2O$, *J. Magn. Reson.*, 1982, **48**, 9–19, DOI: 10.1016/0022-2364(82)90233-5.

46 L. Banci, A. Bencini and D. Gatteschi, Correlation between Anisotropic Exchange and Structure of Di-Mu-Hydroxo Bridged Copper(II) Complexes, *J. Am. Chem. Soc.*, 1983, **105**(4), 761–764, DOI: **10.1021/ja00342a017**.

47 I. Fábián, Hydrolytic Reactions of Copper(II) Bipyridine Complexes, *Inorg. Chem.*, 1989, **28**(20), 3805–3807, DOI: **10.1021/ic00319a011**.

48 M. Judd, G. Jolley, D. Suter, N. Cox and A. Savitsky, Dielectric Coupler for General Purpose Q-Band EPR Cavity, *Appl. Magn. Reson.*, 2022, **53**(7–9), 963–977, DOI: **10.1007/s00723-021-01404-4**.

49 E. Reijerse, F. Lendzian, R. Isaacson and W. Lubitz, A Tunable General Purpose Q-Band Resonator for CW and Pulse EPR/ENDOR Experiments with Large Sample Access and Optical Excitation, *J. Magn. Reson.*, 2012, **214**, 237–243, DOI: **10.1016/j.jmr.2011.11.011**.

50 E. R. Davies, A New Pulse Technique, *Phys. Lett.*, 1974, **47A**(1), 1–2, DOI: **10.1016/0375-9601(74)90078-4**.

51 B. Epel, D. Arieli, D. Baute and D. Goldfarb, Improving W-Band Pulsed ENDOR Sensitivity-Random Acquisition and Pulsed Special TRIPLE, *J. Magn. Reson.*, 2003, **164**, 78–83, DOI: **10.1016/s1090-7807(03)00191-5**.

52 P. Schosseler, T. Wacker and A. Schweiger, Pulsed ELDOR Detected NMR, *Chem. Phys. Lett.*, 1994, **224**, 19–324, DOI: **10.1016/0009-2614(94)00548-6**.

53 S. Stoll and A. Schweiger, EasySpin, a Comprehensive Software Package for Spectral Simulation and Analysis in EPR, *J. Magn. Reson.*, 2006, **178**, 42–55, DOI: **10.1016/j.jmr.2005.08.013**.

54 N. Wili, S. Richert, B. Limburg, S. J. Clarke, H. L. Anderson, C. R. Timmel and G. Jeschke, ELDOR-Detected NMR beyond Hyperfine Couplings: A Case Study with Cu(II)-Porphyrin Dimers, *Phys. Chem. Chem. Phys.*, 2019, **21**(22), 11676–11688, DOI: **10.1039/c9cp01760g**.

55 F. Neese and J. Wiley, The ORCA Program System, *Wiley Interdiscip. Rev.: Comput. Mol. Sci.*, 2012, **2**(1), 73–78, DOI: **10.1002/wcms.81**.

56 F. Neese, Software Update: The ORCA Program System—Version 5.0, *Wiley Interdiscip. Rev.: Comput. Mol. Sci.*, 2022, **12**(5), e1606, DOI: **10.1002/wcms.1606**.

57 S. Grimme, J. Antony, S. Ehrlich and H. Krieg, A Consistent and Accurate Ab Initio Parametrization of Density Functional Dispersion Correction (DFT-D) for the 94 Elements H-Pu, *J. Chem. Phys.*, 2010, **132**(15), 154104, DOI: **10.1063/1.3382344/926936**.

58 S. Grimme, S. Ehrlich and L. Goerigk, Effect of the Damping Function in Dispersion Corrected Density Functional Theory, *J. Comput. Chem.*, 2011, **32**(7), 1456–1465, DOI: **10.1002/jcc.21759**.

59 M. Cossi, N. Rega, G. Scalmani and V. Barone, Energies, Structures, and Electronic Properties of Molecules in Solution with the C-PCM Solvation Model, *J. Comput. Chem.*, 2003, **24**(6), 669–681, DOI: **10.1002/jcc.10189**.

60 E. Van Lenthe, J. G. Snijders and E. J. Baerends, The Zero–order Regular Approximation for Relativistic Effects: The Effect of Spin–Orbit Coupling in Closed Shell Molecules, *J. Chem. Phys.*, 1996, **105**(15), 6505–6516, DOI: **10.1063/1.472460**.

61 E. Van Lenthe, E. J. Baerends and J. G. Snijders, Relativistic Total Energy Using Regular Approximations, *J. Chem. Phys.*, 1994, **101**(11), 9783–9792, DOI: **10.1063/1.467943**.

62 E. Van Lenthe, E. J. Baerends and J. G. Snijders, Relativistic Regular Two–component Hamiltonians, *J. Chem. Phys.*, 1993, **99**(6), 4597–4610, DOI: **10.1063/1.466059**.

63 J. P. Perdew, Density-Functional Approximation for the Correlation Energy of the Inhomogeneous Electron Gas, *Phys. Rev. B: Condens. Matter Mater. Phys.*, 1986, **33**(12), 8822–8824, DOI: **10.1103/physrevb.33.8822**.

64 A. D. Becke, Density-Functional Exchange-Energy Approximation with Correct Asymptotic Behavior, *Phys. Rev. A*, 1988, **38**(6), 3098–3100, DOI: **10.1103/physreva.38.3098**.

65 A. D. Becke, Density–functional Thermochemistry. III. The Role of Exact Exchange, *J. Chem. Phys.*, 1993, **98**(7), 5648–5652, DOI: **10.1063/1.464913**.

66 C. Lee, W. Yang and R. G. Parr, Development of the Colle-Salvetti Correlation-Energy Formula into a Functional of the Electron Density, *Phys. Rev. B: Condens. Matter Mater. Phys.*, 1988, **37**(2), 785, DOI: **10.1103/physrevb.37.785**.

67 F. Weigend, Accurate Coulomb-Fitting Basis Sets for H to Rn, *Phys. Chem. Chem. Phys.*, 2006, **8**(9), 1057–1065, DOI: **10.1039/b515623h**.

68 F. Weigend and R. Ahlrichs, Balanced Basis Sets of Split Valence, Triple Zeta Valence and Quadruple Zeta Valence Quality for H to Rn: Design and Assessment of Accuracy, *Phys. Chem. Chem. Phys.*, 2005, **7**(18), 3297–3305, DOI: **10.1039/b508541a**.

69 V. Barone, Structure, Magnetic Properties and Reactivities of Open-Shell Species From Density Functional and Self-Consistent Hybrid Methods, in *Recent Advances in Density Functional Methods*, ed. D. P. Chong, World Scientific, Singapore, 1995, pp. 287–334. DOI: **10.1142/9789812830586_0008**.

70 N. Rega, M. Cossi and V. Barone, Development and Validation of Reliable Quantum Mechanical Approaches for the Study of Free Radicals in Solution, *J. Chem. Phys.*, 1996, **105**(24), 11060–11067, DOI: **10.1063/1.472906**.

71 N. B. Balabanov and K. A. Peterson, Systematically Convergent Basis Sets for Transition Metals. I. All-Electron Correlation Consistent Basis Sets for the 3d Elements Sc-Zn, *J. Chem. Phys.*, 2005, **123**(6), 064107, DOI: **10.1063/1.1998907/932754**.

72 E. D. Hedegård, J. Kongsted and S. P. A. Sauer, Optimized Basis Sets for Calculation of Electron Paramagnetic Resonance Hyperfine Coupling Constants: Aug-Cc-PVTZ-J for the 3d Atoms Sc-Zn, *J. Chem. Theory Comput.*, 2011, **7**(12), 4077–4087, DOI: **10.1021/ct200587k**.

73 G. L. Stoychev, A. A. Auer and F. Neese, Automatic Generation of Auxiliary Basis Sets, *J. Chem. Theory Comput.*, 2017, **13**(2), 554–562, DOI: **10.1021/acs.jctc.6b01041**.

74 S. Barnett, *Development and Mechanistic Study of Copper-Based Water Oxidation Catalysts*, Ph. D. Dissertation,

University of Washington, Seattle, WA, 2013. https://digital.lib.washington.edu/researchworks/items/77d25f7b-15b9-4efc-8727-4dce8d5558d3 (accessed 21.09.2024).

75 Y. Y. H. Chao and D. R. Kearns, Electron Spin Resonance Investigation of the Soluble Blue Copper(II) Hydroxide Complex, *J. Phys. Chem.*, 1977, **81**(7), 666–668, DOI: 10.1021/j100522a016.

76 P. C. Bruzzese, E. Salvadori, B. Civalleri, S. Jäger, M. Hartmann, A. Pöppl and M. Chiesa, The Structure of Monomeric Hydroxo-CuII Species in Cu-CHA. A Quantitative Assessment, *J. Am. Chem. Soc.*, 2022, **144**(29), 13079–13083, DOI: 10.1021/jacs.2c06037.

77 M. M. Werst, C. E. Davoust and B. M. Hoffman, Ligand Spin Densities in Blue Copper Proteins by Q-Band 1H and 14N ENDOR Spectroscopy, *J. Am. Chem. Soc.*, 1991, **113**(5), 1533–1538, DOI: 10.1021/ja00005a011.

78 J. E. Roberts, J. F. Cline, V. Lum, H. Freeman, H. B. Gray, J. Peisach, B. Reinhammar and B. Hoffman, Comperative ENDOR Study of Six Blue Copper Proteins, *J. Am. Chem. Soc.*, 1984, **106**, 5324–5330, DOI: 10.1021/ja00330a048.

79 J. A. J. Fitzpatrick, F. R. Manby and C. M. Western, The Interpretation of Molecular Magnetic Hyperfine Interactions, *J. Chem. Phys.*, 2005, **122**(8), 084312, DOI: 10.1063/1.1851501.

80 N. Cox, W. Lubitz and A. Savitsky, W-Band, ELDOR-Detected NMR (EDNMR) Spectroscopy as a Versatile Technique for the Characterisation of Transition Metal-Ligand Interactions, *Mol. Phys.*, 2013, **111**(18–19), 2788–2808, DOI: 10.1080/00268976.2013.830783.

81 N. Cox, W. Lubitz and A. Savitsky, W-Band, ELDOR-Detected NMR (EDNMR) Spectroscopy as a Versatile Technique for the Characterisation of Transition Metal-Ligand Interactions, *Mol. Phys.*, 2013, **111**(18–19), 2788–2808, DOI: 10.1080/00268976.2013.830783.

82 A. R. Lorenz, J. Ammeter and H. H. Günthard, 17O Hyperfine Structure in ESR Spectra of Cu(II) Hydroxyquinolinate: Phthalimide, *Chem. Phys. Lett.*, 1972, **16**(2), 275–277.

83 A. R. Lorenz, J. H. Ammeter and H. H. Günthard, 17O Hyperfine Structure in Single Crystal ESR Spectra of Cu(II) Picolinate:Zn(II) Picolinate·4H_2O, *Chem. Phys. Lett.*, 1973, **23**(4), 463–466.